Check for updates

View Article Online
View Journal

Chemical Science

Accepted Manuscript

This article can be cited before page numbers have been issued, to do this please use: T. Sirirat, S. Janprakhon, N. Joraleechanchai, S. Prempluem, S. Duangdangchote and M. Sawangphruk, *Chem. Sci.*, 2026, DOI: 10.1039/D6SC03512D.

This is an Accepted Manuscript, which has been through the Royal Society of Chemistry peer review process and has been accepted for publication.

Accepted Manuscripts are published online shortly after acceptance, before technical editing, formatting and proof reading. Using this free service, authors can make their results available to the community, in citable form, before we publish the edited article. We will replace this Accepted Manuscript with the edited and formatted Advance Article as soon as it is available.

You can find more information about Accepted Manuscripts in the Information for Authors.

Please note that technical editing may introduce minor changes to the text and/or graphics, which may alter content. The journal's standard Terms & Conditions and the Ethical guidelines still apply. In no event shall the Royal Society of Chemistry be held responsible for any errors or omissions in this Accepted Manuscript or any consequences arising from the use of any information it contains.

ROYAL SOCIETY OF CHEMISTRY

rsc.li/chemical-science

View Article Online
DOI: 10.1039/D6SC03512D

When Fluorination Becomes Inactive: Solvation Exclusion and Interfacial Kinetics in Ni-Rich Lithium-Ion Batteries

Thanitsavat Sirirat, Sukritta Janprakhon, Nattanon Joraleechanchai, Surat Prempluem, Salatan Duangdangchote and Montree Sawangphruk*

Centre of Excellence for Energy Storage Technology, Department of Chemical and Biomolecular Engineering, School of Energy Science and Engineering, Vidyasirimedhi Institute of Science and Technology, Rayong 21210, Thailand

*E-mail: montree.s@vistec.ac.th

Open Access Article. Published on 22 June 2026. Downloaded on 6/23/2026 5:02:46 AM.
This article is licensed under a Creative Commons Attribution-NonCommercial 3.0 Unported Licence.

Chemical Science Accepted Manuscript

Abstract

Fluorinated carbonate additives are widely employed to stabilize electrolytes for high-energy lithium-ion batteries (LIBs), yet the interplay between fluorination degree, molecular geometry, and lithium-ion (Li^+) solvation remains poorly understood. It is commonly assumed that increasing fluorination uniformly weakens Li^+ solvation and improves interfacial stability. Here, we demonstrate that excessive fluorination—particularly in linear carbonate additives—can instead render the additives solvation-inactive through a previously unrecognized mechanism termed solvation exclusion. In this regime, highly fluorinated linear additives are expelled from the Li^+ first solvation shell, leading to kinetically unfavorable interfacial processes. Using a multiscale approach integrating density functional theory, molecular dynamics simulations, multinuclear DOSY NMR, temperature-dependent electrochemical impedance spectroscopy, and long-term NMC90‖graphite full-cell testing, we systematically compare cyclic and linear fluorinated carbonates with graded fluorination. We reveal that cyclic carbonates with moderate fluorination

View Article Online
DOI: 10.1039/D6SC03512D

Open Access Article. Published on 22 June 2026. Downloaded on 6/23/2026 5:02:46 AM.
This article is licensed under a Creative Commons Attribution-NonCommercial 3.0 Unported Licence.

remain active in Li^+ solvation, promote controlled contact-ion-pair formation, lower charge-transfer activation energies, and form LiF-rich, mechanically robust interphases. Conversely, highly fluorinated linear additives trigger solvation exclusion, resulting in elevated activation barriers, organic-rich interphases, severe cathode cracking, and rapid capacity fading. Furthermore, galvanostatic intermittent titration measurements confirm that these performance disparities stem strictly from interfacial kinetics rather than bulk lithium diffusion. These findings establish that optimal electrolyte design requires balancing the fluorination degree and molecular geometry to preserve active solvation participation. Ultimately, this work provides fundamental insights and practical design principles for developing robust fluorinated electrolytes for Ni-rich LIBs, particularly under high-rate and low-temperature operations.

Keywords; Fluorinated electrolytes; Solvation exclusion; Interfacial kinetics; Li^+ solvation structure; Ni-rich lithium-ion batteries

1. Introduction

Lithium-ion batteries (LIBs) are indispensable for portable electronics and electric vehicles (EVs) owing to their high energy density, long cycle life, and scalable manufacturing infrastructure [1-5]. To meet the growing demand for higher energy density, Ni-rich layered oxide cathodes, such as NMC and NCA compositions, have been widely adopted because of their high reversible capacities exceeding 200 mAh g^{-1}. However, as these cathodes are pushed toward higher operating voltages (>4.3 V) and higher current densities, they approach fundamental electrochemical and mechanical limits. Severe structural degradation and interfacial instability—including lattice oxygen release, surface reconstruction, and transition-metal migration—are frequently observed, leading to rapid capacity fading and shortened cycle life [6-8]. These degradation processes are

Chemical Science Accepted Manuscript

View Article Online
DOI: 10.1039/D6SC03512D

Open Access Article. Published on 22 June 2026. Downloaded on 6/23/2026 5:02:46 AM.
This article is licensed under a Creative Commons Attribution-NonCommercial 3.0 Unported Licence.

Chemical Science Accepted Manuscript

further exacerbated by conventional carbonate-based electrolytes (EC, DEC, DMC, EMC), which suffer from limited oxidative stability and sluggish lithium-ion (Li^+) transport, resulting in high polarization and unfavorable interfacial kinetics at elevated voltages. Consequently, electrolyte design has emerged as a critical bottleneck in unlocking the full performance potential of Ni-rich cathodes in next-generation high-energy LIBs [9, 10].

Electrolyte engineering, particularly through the use of fluorinated carbonate additives, has become a central strategy to mitigate interfacial degradation and improve electrochemical stability. Cyclic fluorinated carbonates such as fluoroethylene carbonate (FEC) and difluoroethylene carbonate (DFEC), as well as linear analogues including FDEC, DFDEC, TFDEC, and TTFDEC, have been widely explored as effective additives for stabilizing the solid–electrolyte interphase (SEI), suppressing parasitic reactions, and improving Li^+ transport [11-16]. Owing to the strong electron-withdrawing nature of fluorine, fluorinated solvents can modulate the electrolyte solvation environment, widen the electrochemical stability window, and alter Li^+–solvent interactions [5, 17]. Numerous studies have shown that moderate fluorination can lower melting points, enhance ionic conductivity, and improve Li^+ mobility by stabilizing favorable solvation structures [18, 19]. Although, when fluorination is increased at a fixed high additive concentration, electrolytes containing highly fluorinated linear additives often exhibit pronounced capacity loss and severe instability, particularly during the formation process, indicating that excessive fluorination at high concentrations can be detrimental to cell performance [20].

The phenomenon of intentional solvation exclusion is well established in the context of localized high-concentration electrolytes (LHCEs), where non-solvating fluorinated diluents—such as bis(2,2,2-trifluoroethyl) ether (BTFE) and 1,1,2,2-tetrafluoroethyl-2,2,3,3-tetrafluoropropyl ether (TTE)—are deliberately excluded from the Li^+ first solvation shell at molar salt concentrations

View Article Online
DOI: 10.1039/D6SC03512D

Open Access Article. Published on 22 June 2026. Downloaded on 6/23/2026 5:02:46 AM.
This article is licensed under a Creative Commons Attribution-NonCommercial 3.0 Unported Licence.

exceeding 3–4 M, thereby preserving the concentrated solvation clusters of the parent high-concentration electrolyte (HCE). However, analogous solvation-exclusion effects in dilute (≤1 M) additive-level systems, where the fluorinated species constitutes only 3–25 vol% of a conventional carbonate electrolyte, have not been systematically investigated. These counterintuitive results challenge the prevailing assumption that weaker solvation arising from fluorination universally facilitates Li^+ desolvation and charge-transfer kinetics. Indeed, ab initio and MD studies on fluorinated linear carbonates, including fluorinated ethyl methyl carbonates (F*n*EMC, n = 1–3), have shown that Li^+–solvent binding energy decreases progressively with fluorination degree, and that highly fluorinated variants contribute negligibly to the Li^+ coordination shell. Instead, excessive fluorination can weaken Li^+–solvent binding to such an extent that the additive barely participates in the first solvation shell, effectively rendering it solvation-inactive and giving rise to rigid, poorly conducting solvation structures that degrade overall electrochemical performance [24]. A fundamental question therefore remains unresolved: does excessive fluorination fundamentally alter the role of an additive in the Li^+ solvation environment, and how does molecular geometry (cyclic versus linear) govern this behavior?

Despite extensive research on fluorinated electrolytes, a systematic understanding of how fluorination degree and molecular topology jointly determine Li^+ solvation, ion-pairing behavior, and interfacial kinetics in Ni-rich full cells is still lacking. Most prior studies focus on isolated additives, low-temperature operation, or single performance metrics such as SEI composition or ionic conductivity, or exploit solvation exclusion by design in HCE/LHCE regimes at salt concentrations far exceeding 1 M. Critically, in the LHCE paradigm, solvation exclusion is an engineered and beneficial feature enabled by high salt-to-solvent ratios; in contrast, the accidental or unintended exclusion of an additive at low concentration in a conventional 1 M electrolyte has

Chemical Science Accepted Manuscript

View Article Online
DOI: 10.1039/D6SC03512D

Open Access Article. Published on 22 June 2026. Downloaded on 6/23/2026 5:02:46 AM.
This article is licensed under a Creative Commons Attribution-NonCommercial 3.0 Unported Licence.

not been recognized as a distinct failure mechanism, nor has it been systematically characterized across a graded series of cyclic and linear fluorinated carbonates. Furthermore, prior comparisons of FEC and its linear analogues have been limited in scope, examining only one or two additives at fixed or non-matched concentrations without establishing a unified structure–solvation–kinetics relationship. No prior study has simultaneously quantified the electronic, steric, and thermodynamic descriptors governing Li^+–additive binding across a structurally matched cyclic and linear series, nor linked these molecular-level descriptors to long-term full-cell performance under realistic operating conditions. Addressing this gap requires a multiscale approach that integrates molecular-level solvation analysis with long-term electrochemical performance in practical cell configurations.

While unraveling the fundamental solvation structures of novel electrolytes is scientifically crucial, the ultimate goal of advanced electrolyte design is to overcome practical engineering challenges in high-energy-density lithium-ion batteries. Specifically, modern applications demand electrolytes that can operate reliably under extreme conditions, such as fast-charging scenarios and low-temperature climates. Understanding the precise molecular behavior of fluorinated additives—particularly how they participate in or are excluded from the primary Li^+ solvation shell—provides a critical foundation for rationally designing electrolytes that facilitate rapid desolvation kinetics and address these real-world operational bottlenecks.

In this work, we systematically investigate the effects of fluorination degree and molecular geometry on electrolyte functionality using both cyclic (FEC, DFEC) and linear fluorinated carbonates (FDEC, DFDEC, TFDEC, and TTFDEC) in a conventional 1 M $LiPF_6$ in EC: DEC: DMC (1:1:1) electrolyte. As conceptually illustrated in Figure 2, we distinguish two fundamentally different solvation regimes: (i) *active solvation*, in which the additive occupies a coordination site

Chemical Science Accepted Manuscript

View Article Online
DOI: 10.1039/D6SC03512D

Open Access Article. Published on 22 June 2026. Downloaded on 6/23/2026 5:02:46 AM.
This article is licensed under a Creative Commons Attribution-NonCommercial 3.0 Unported Licence.

within the Li^+ first solvation shell (typified by FEC and FDEC, CN ≈ 0.6–0.7), and (ii) *solvation exclusion*, in which the additive resides beyond the primary coordination sphere due to combined steric and electronic penalties (typified by TFDEC and TTFDEC, CN ≈ 0.004–0.04). This distinction is absent in the LHCE literature, where exclusion is enforced by salt-excess thermodynamics rather than intrinsic molecular properties. By combining density functional theory (DFT)—including natural bond orbital (NBO) analysis, percent buried volume ($\%V_{Bur}$), and cluster desolvation energy calculations—molecular dynamics (MD) simulations, multinuclear DOSY NMR, electrochemical characterization, and post-mortem analysis in NMC90/graphite full cells, we reveal that excessive fluorination in linear carbonates causes solvation exclusion through steric rather than purely electronic origin. This exclusion produces rigid, kinetically trapped solvation structures with high charge-transfer activation energies and poor interfacial stability. In contrast, cyclic fluorinated carbonates with balanced fluorination maintain active participation in Li^+ solvation, promote controlled contact-ion-pair formation, enable LiF-rich and mechanically robust interphases, and deliver superior rate capability and long-term cycling stability. To decouple fluorination effects from simple concentration scaling, additive concentrations were scaled inversely with fluorination degree (25 vol% for monofluorinated → 3.125 vol% for tetrafluorinated), thereby avoiding instability in highly fluorinated systems while preserving meaningful fluorination trends within each additive series. These findings establish that optimal electrolyte design for Ni-rich LIBs requires not maximized fluorination, but a balance between fluorination degree and molecular geometry to preserve active solvation participation and favorable interfacial kinetics—a design principle that is fundamentally distinct from the concentration-driven exclusion exploited in LHCE systems.

Chemical Science Accepted Manuscript

View Article Online
DOI: 10.1039/D6SC03512D

Open Access Article. Published on 22 June 2026. Downloaded on 6/23/2026 5:02:46 AM.
This article is licensed under a Creative Commons Attribution-NonCommercial 3.0 Unported Licence.

2. Experimental Section

2.1 Electrode Preparation

Coin cells were fabricated using Ni-rich layered oxide cathode material (NMC90, $LiNi_{0.9}Mn_{0.05}Co_{0.05}O_2$) supplied by Gelon Lib Group Co., Ltd. (China). The cathode slurry was prepared by mixing 95.2 wt% NMC90 active material, 2.4 wt% polyvinylidene fluoride (PVDF, Aldrich) as the binder, and 2.4 wt% conductive carbon black (Super P, Alfa Aesar) in N-methyl-2-pyrrolidone (NMP, QREC) as the solvent. The components were homogenized using mechanical stirring until a uniform slurry was obtained. The resulting slurry was coated onto aluminum foil (current collector) using a doctor-blade technique and dried in a convection oven at 80 °C overnight to remove residual solvent. After drying, the electrodes were calendered to a thickness of 200 μm to achieve consistent electrode density and interparticle contact. Circular cathode disks with a diameter of 14 mm were then punched from the coated foil. The resulting cathodes exhibited an active material mass loading of approximately 31.62 mg cm^{-2}. The crystallographic phase purity and layered structure of the as-received NMC90 powder were verified by X-ray diffraction (XRD), as shown in Figure S1, confirming its suitability for electrochemical evaluation.

2.2 Electrolyte Preparation using fluorinated Solvent

All electrolyte solutions were prepared by weight in an argon filled glovebox (MBRAUN, Germany), maintaining an environment with water (H_2O) and oxygen (O_2) levels below 0.1 ppm to ensure the purity and stability of the solution. The base electrolyte solvent consisted of ethylene carbonate (EC), dimethyl carbonate (DMC), and diethyl carbonate (DEC) mixed in a 1:1:1 weight ratio, with all carbonate solvents supplied by Gelon Lib Group Co., Ltd. (China) and used as received. The low moisture content of the solvents (<20 ppm) was verified by the supplier and

Chemical Science Accepted Manuscript

View Article Online
DOI: 10.1039/D6SC03512D

Open Access Article. Published on 22 June 2026. Downloaded on 6/23/2026 5:02:46 AM.
This article is licensed under a Creative Commons Attribution-NonCommercial 3.0 Unported Licence.

ensured to prevent electrolyte degradation or hydrogen evolution during cell operation. The electrolyte salt, lithium hexafluorophosphate ($LiPF_6$, 1 M), was also purchased from Gelon Lib Group Co., Ltd. and dried according to the supplier's specifications prior to use. Fluorinated cyclic carbonate additives, FEC and DFEC were obtained from Gelon Lib Group Co., Ltd., whereas FDEC, DFDEC, TFDEC, and TTFDEC were obtained from Shanghai Ji Zhao Information Technology Co., Ltd., ensuring consistency in purity and synthesis route across all electrolyte formulations, For electrolyte preparation, $LiPF_6$ was first gradually dissolved in the EC:DMC:DEC solvent mixture under continuous stirring until a clear and homogeneous solution was obtained. The desired fluorinated additive was then introduced at the specified volume fraction and the electrolyte was stirred overnight to ensure complete dissolution and uniform composition. The final electrolyte formulations used for electrochemical testing of NMC90/graphite coin cells are summarized in Table S1. Electrolyte wetting and uptake were evaluated using a 2000 μL flood-volume test, as detailed in Table S2 and Figure S2, which confirmed that an electrolyte volume of 100 μL per CR2032 coin cell is sufficient to fully wet the electrodes and separators and to maintain stable ionic transport throughout electrochemical testing. To account for the increasing degree of molecular fluorination and to avoid electrochemical instability associated with highly fluorinated linear carbonates, the additive concentrations were scaled inversely with the number of fluorine atoms per molecule (25 vol% for mono-fluorinated, 12.5 vol% for di-fluorinated, 6.25 vol% for tri-fluorinated, and 3.12 vol% for tetra-fluorinated species). Specifically, each fluorinated additive was added to the baseline electrolyte (denoted as REF), which comprised 1.0 M $LiPF_6$ in EC:DEC:DMC (1:1:1 by volume) and served as the control sample for all comparative analyses. This strategy preserves comparable fluorination trends within each additive series while intentionally not enforcing identical total fluorine content across all electrolyte formulations.

Chemical Science Accepted Manuscript

View Article Online
DOI: 10.1039/D6SC03512D

Open Access Article. Published on 22 June 2026. Downloaded on 6/23/2026 5:02:46 AM.
This article is licensed under a Creative Commons Attribution-NonCommercial 3.0 Unported Licence.

2.3 Coin Cell Assembly

Prior to cell assembly, 14 mm diameter cathode electrodes and 15.5 mm diameter anode electrodes were vacuum-dried at 80 °C overnight to remove residual moisture and adsorbed solvents. All coin cells were assembled in an argon-filled glovebox with H_2O and O_2 levels maintained below 0.1 ppm. CR2032-type coin cells were assembled in both full-cell and half-cell configurations. For NMC90/graphite full cells, the cell stack consisted of a graphite negative electrode, two layers of microporous polypropylene separator (Celgard-type), and an NMC90 positive electrode. For half-cell measurements, the stack comprised an NMC90 cathode, two separators, and a lithium metal foil disk (Gelon Lib Group Co., Ltd.) serving as the counter and reference electrode. An excess electrolyte volume of 100 μL per cell was added to each coin cell to ensure complete wetting of the electrodes and separators, consistent with the electrolyte uptake analysis presented in Table S2. After electrolyte addition, the cells were sealed using a hydraulic crimping machine. A schematic illustration of the CR2032 coin-cell configuration and assembly procedure is provided in Figure S3.

2.4 Electrochemical Formation Protocols

Galvanostatic charge–discharge (GCD) cycling was carried out using a battery testing system (Gelon Lib Group Co., Ltd.) at a controlled temperature of 25 °C. All electrochemical tests were performed on CR2032 coin cells following a defined preconditioning and formation procedure. Prior to electrochemical cycling, the assembled cells were rested at an open-circuit voltage of approximately 1.5 V for 12 h to ensure uniform electrolyte wetting and interfacial stabilization. The cells were then subjected to a formation process consisting of constant-current–constant-

Chemical Science Accepted Manuscript

View Article Online
DOI: 10.1039/D6SC03512D

Open Access Article. Published on 22 June 2026. Downloaded on 6/23/2026 5:02:46 AM.
This article is licensed under a Creative Commons Attribution-NonCommercial 3.0 Unported Licence.

voltage (CCCV) charging to 4.3 V at a C/20 rate, followed by CCCV discharging to 3.0 V at C/20. The constant-voltage step during charging was terminated when the current decayed to C/50. In this work, 1C was defined as 212 mAh g^{-1}, corresponding to the theoretical capacity of the NMC90 cathode. After the formation cycles, long-term electrochemical testing was conducted under CCCV conditions by charging to 4.2 V at C/10 and discharging to 3.0 V at C/10. All cycling tests were performed at 25 °C unless otherwise specified.

2.5 Galvanostatic intermittent titration technique

Galvanostatic intermittent titration technique (GITT) measurements were performed in a half-cell CR2032 coin-cell configuration. NMC90 cathode electrodes were assembled against lithium metal foil (Gelon Lib Group Co., Ltd.) as the counter and reference electrode in an argon-filled glovebox (MBRAUN UNILAB, Germany; H_2O and O_2 < 0.1 ppm). The electrode composition and preparation were identical to those used in the full-cell configuration described above. During GITT measurements, the cells were subjected to a series of galvanostatic current pulses at 0.1C for 10 min, followed by a 30 min relaxation period at open circuit to allow the cell voltage to approach equilibrium. The GITT protocol was applied sequentially during both charge and discharge processes within the voltage window of 3.0–4.3 V (vs Li^+/Li). All measurements were conducted at 25 °C. The chemical diffusion coefficient of lithium ions (D□) in the NMC90 cathode was calculated using the following equation:

$$D_S = \frac{4}{\pi\tau}\left(\frac{m_B V_M}{M_B A}\right)^2\left(\frac{\Delta E_s}{\Delta E_\tau}\right)^2 \quad (1)$$

where D_s is the chemical diffusion coefficient of Li^+, τ is the duration of the current pulse (600 s), m_B is the mass of active material in the cathode, M_B is the molar mass of the active material, V_M

Chemical Science Accepted Manuscript

View Article Online
DOI: 10.1039/D6SC03512D

Open Access Article. Published on 22 June 2026. Downloaded on 6/23/2026 5:02:46 AM.
This article is licensed under a Creative Commons Attribution-NonCommercial 3.0 Unported Licence.

is the molar volume of the active material, A is the effective contact area between the electrode and electrolyte, ΔE_s is the steady-state voltage change during the relaxation period, and ΔE_τ is the voltage change during the constant-current pulse after eliminating the initial iR drop. This analysis assumes that the molar volume V_M remains constant during electrochemical cycling. The effective contact area A was estimated based on the geometric electrode area and the specific surface area of the active material obtained from BET measurements. The molar volume V_M was determined using three independent approaches: (i) calculation from the true density of the NMC90 powder, (ii) calculation from the measured electrode density, and (iii) calculation from crystallographic parameters (lattice constants *a* and *c*) obtained via XRD Rietveld refinement. Consistent values obtained from these methods confirmed the reliability of the diffusion coefficient analysis.

2.6 Simulation Details

Classical molecular dynamics (MD) simulations were performed to investigate lithium-ion solvation structures and transport properties using the Optimized Potentials for Liquid Simulations–All Atom (OPLS-AA) force field. All bonded interactions, including bond stretching, angle bending, dihedral torsions, and improper torsions, were explicitly described within the OPLS-AA framework. Partial atomic charges for all solvent molecules, fluorinated additives, and ions were derived using density functional theory (DFT) calculations. Molecular geometries were first fully optimized using Becke's three-parameter hybrid exchange functional combined with the Lee–Yang–Parr correlation functional (B3LYP) with the 6-311G++(2d,2p) basis set, as implemented in Gaussian 16. Electrostatic potentials were subsequently calculated via single-point energy evaluations, and Restrained Electrostatic Potential (RESP) fitting was employed to assign partial charges compatible with the OPLS-AA force field. Cubic simulation boxes were

Chemical Science Accepted Manuscript

View Article Online
DOI: 10.1039/D6SC03512D

Open Access Article. Published on 22 June 2026. Downloaded on 6/23/2026 5:02:46 AM.
This article is licensed under a Creative Commons Attribution-NonCommercial 3.0 Unported Licence.

constructed using WinMolStar based on an experimentally relevant electrolyte density of 1.29 g cm^{-3}. Each simulation cell contained Li^+ and PF_6^- ions together with carbonate solvents (EC, DEC, DMC) and the corresponding fluorinated additive. The exact number of molecules in each system is summarized in Table S3, ensuring identical salt concentration and comparable solvent compositions across all simulations. Initial configurations were subjected to energy minimization using a conjugate-gradient algorithm for 20,000 steps to eliminate unfavorable contacts. The systems were then equilibrated in the isothermal–isobaric (NPT) ensemble at 300 K and 1 bar for 2 ns with a time step of 0.5 fs, allowing the cell volume to relax to the target density. Following equilibration, production MD simulations were carried out in the canonical (NVT) ensemble at 300 K for 20 ns using a time step of 1 fs. Periodic boundary conditions were applied in all three dimensions. Trajectory analysis was performed using the final 4 ns of the production runs. To ensure the statistical reliability of the structural analysis, the system's convergence was strictly validated using block average analysis. As shown in Figure S4, the standard errors of temperature and pressure plateaued completely, confirming full temporal decorrelation. Consequently, only the final 4 ns of this highly converged 20 ns trajectory were extracted for the coordination number analysis, effectively eliminating initial memory effects and guaranteeing a statistically mature ensemble. All MD simulations and analyses were conducted using the GROMACS simulation package on an 18-core Unix-based computing cluster.

2.7 Electrochemical impedance spectroscopy (EIS)

Electrochemical impedance spectroscopy (EIS) measurements were conducted in CR2032-type coin half-cell configurations using an AUTOLAB PGSTAT302N electrochemical workstation. All measurements were performed under controlled temperature conditions using an environmental

Chemical Science Accepted Manuscript

View Article Online
DOI: 10.1039/D6SC03512D

Open Access Article. Published on 22 June 2026. Downloaded on 6/23/2026 5:02:46 AM.
This article is licensed under a Creative Commons Attribution-NonCommercial 3.0 Unported Licence.

chamber. Impedance spectra were recorded over a frequency range of 100 kHz to 0.01 Hz with an applied AC perturbation amplitude of 10 mV. Temperature-dependent EIS measurements were carried out at −10, 0, 10, 20, and 30 °C to evaluate interfacial charge-transfer kinetics. Prior to each measurement, the cells were equilibrated at the target temperature for at least 2 h to ensure thermal and electrochemical stabilization. For cathode half-cell measurements, the cells were held at a constant potential of 3.88 V vs Li^+/Li, while for anode (graphite) half-cell measurements, the cells were held at 0.099 V vs Li^+/Li, corresponding to approximately 50% state of charge (SOC). These potentials were selected to minimize phase-transition effects and to probe charge-transfer resistance under representative operating conditions.

The activation energy (E_a) was obtained by fitting the temperature dependence of the charge-transfer resistance (R_{ct}) using the Arrhenius relation:

$$R_{ct} = A\, exp\left(\frac{E_a}{k_B T}\right) \qquad (2)$$

where A is the pre-exponential Arrhenius constant, kB is the Boltzmann constant, and T is the temperature in Kelvin.

2.8 ^{7}Li and ^{19}F DOSY NMR

To quantify ion diffusion coefficients in electrolyte solutions, two-dimensional Diffusion-Ordered Spectroscopy (DOSY) NMR was performed following electrochemical cycling. Electrolyte samples (35 µL) were diluted to 700 µL with deuterated dimethyl sulfoxide (DMSO-d_6) to ensure optimal signal-to-noise ratio and field locking. The NMR sample setup is shown in Figure S5. ^{7}Li and ^{19}F DOSY NMR spectra were acquired on a Bruker Ascent 600 MHz spectrometer equipped with a cryoprobe for enhanced sensitivity. The pulse sequence for DOSY was repeated across a

Chemical Science Accepted Manuscript

View Article Online
DOI: 10.1039/D6SC03512D

range of magnetic field gradient strengths. The resulting spectra exhibited attenuation of signal intensities as a function of gradient, governed by the Stejskal–Tanner equation:

$$S(t) = S(0) \times exp[-D\gamma^2 g^2 \delta^2 (\Delta - \frac{\delta}{3})] \qquad (3)$$

- **S(t)**: NMR signal intensity after applying the gradient pulse.
- **S(0)**: Initial NMR signal intensity without gradient.
- **D**: Diffusion coefficient of the molecule.
- **γ**: Gyromagnetic ratio of the nucleus being observed.
- **g**: Strength of the applied magnetic field gradient.
- **δ**: Duration of the gradient pulse.
- **Δ**: Time between the start of two gradient pulses (diffusion time).

As these parameters are all known, the logarithm of the signal can be plotted to obtain a linear decay against $\gamma^2.g^2.\delta^2.(\Delta-\delta/3)$ with slope -D, the diffusion coefficient D was extracted from the slope. All DOSY data were processed and fitted using Bruker TopSpin and Dynamics Center software.

3. Results and discussion

3.1 Fluorination-Dependent Li^+ Solvation: Electronic Structure, Binding Strength, and Transport Signatures

To elucidate how fluorination modulates Li^+ solvation and transport behavior, we first examined the electronic structure of carbonate solvents and fluorinated additives using DFT. As shown in Figure 1a, fluorination induces a pronounced electron-withdrawing effect on the carbonyl oxygen atoms, which serve as the primary Li^+ coordination sites. With increasing fluorination, the partial negative charge on the carbonyl oxygen systematically decreases, from −0.434 in EC through the cyclic series (FEC: −0.431; DFEC: −0.426), and from −0.421 in DEC through the linear series

Open Access Article. Published on 22 June 2026. Downloaded on 6/23/2026 5:02:46 AM.
This article is licensed under a Creative Commons Attribution-NonCommercial 3.0 Unported Licence.

Chemical Science Accepted Manuscript

View Article Online
DOI: 10.1039/D6SC03512D

Open Access Article. Published on 22 June 2026. Downloaded on 6/23/2026 5:02:46 AM.
This article is licensed under a Creative Commons Attribution-NonCommercial 3.0 Unported Licence.

(FDEC: −0.419; DFDEC: −0.417; TFDEC: −0.414), ultimately reaching −0.412 in TTFDEC. This progressive charge depletion weakens the Lewis basicity of the carbonyl oxygen toward Li^+, directly altering the strength and nature of Li^+–solvent interactions within the primary solvation shell [25]. The molecular structures and relevant physicochemical properties of the fluorinated additives are summarized in Table S4. To complement this Mulliken-type charge analysis, natural bond orbital (NBO) calculations were also performed (Figure S6). The NBO charges on the carbonyl oxygen vary only modestly across the series, from approximately -0.900 for FEC to -0.935 for TTFDEC, a range considerably narrower than the trend implied by the ESP maps. This near-invariance of NBO charge confirms that fluorination reshapes the electrostatic surface potential primarily through through-space inductive effects rather than through direct depletion of the carbonyl lone pairs, and underscores that electronic descriptors alone are insufficient to explain the dramatic differences in Li^+ coordination observed between cyclic and highly fluorinated linear carbonates.

Consistent with the electrostatic potential analysis, DFT-calculated Li^+–solvent binding energies (Figure 1b) further quantify the impact of fluorination on coordination strength. Among all solvents, FEC exhibits the strongest Li^+ binding energy (−0.64 eV), reflecting robust Li–O coordination through the carbonyl group. In contrast, DFEC, FDEC, and DFDEC show intermediate and relatively similar binding energies (−0.53, −0.51, and −0.48 eV, respectively), indicating that moderate fluorination—regardless of cyclic or linear geometry—preserves effective Li^+ coordination. Notably, highly fluorinated linear carbonates, TFDEC and TTFDEC, display substantially weaker binding energies (−0.33 and −0.25 eV), implying excessively weakened Li^+–solvent interactions that hinder their participation in the first solvation shell [26].

Chemical Science Accepted Manuscript

View Article Online
DOI: 10.1039/D6SC03512D

Open Access Article. Published on 22 June 2026. Downloaded on 6/23/2026 5:02:46 AM.
This article is licensed under a Creative Commons Attribution-NonCommercial 3.0 Unported Licence.

Because solvents directly coordinated with Li^+ are preferentially reduced at electrode surfaces to form the solid–electrolyte interphase (SEI) [27], such changes in solvation structure are expected to have important electrochemical consequences. Experimental evidence for fluorination-induced solvation modifications is provided by the ^7Li NMR spectra shown in Figure 1c, with complementary ^{19}F NMR data presented in Figure S7. The reproducibility of the DOSY NMR measurements is confirmed by consistent spectra across three independent replicates (Figure S8). Relative to the reference electrolyte (−0.55 ppm), electrolytes containing cyclic fluorinated additives exhibit clear upfield shifts (FEC + REF: −0.57 ppm; DFEC + REF: −0.59 ppm), consistent with increased participation of PF_6^- anions in the Li^+ solvation shell and a concomitant weakening of Li^+–solvent coordination.

In contrast, as fluorination increases in the linear carbonate series, the ^7Li resonance shifts progressively downfield (FDEC + REF: −0.56 ppm; DFDEC + REF: −0.52 ppm; TFDEC + REF: −0.51 ppm; TTFDEC + REF: −0.50 ppm), which would conventionally be interpreted as enhanced Li^+–solvent interactions. However, molecular dynamics (MD) simulations (Figure 2 and Table 1) reveal that this apparent trend masks a fundamentally different mechanism. Owing to the lower electron-donating capability of DEC-based linear carbonates compared to EC-based cyclic species (as reflected in the ESP analysis in Figure 1a), highly fluorinated linear additives such as TFDEC and TTFDEC are increasingly excluded from the Li^+ coordination environment. At additive concentrations of 6.25 vol% (TFDEC) and 3.12 vol% (TTFDEC), these molecules contribute negligibly to the first solvation shell, which instead becomes dominated by conventional carbonates (EC, DMC, and DEC). This solvation exclusion, rather than strengthened coordination, reconciles the NMR observations and is directly linked to the altered interfacial kinetics observed in subsequent electrochemical measurements.

Chemical Science Accepted Manuscript

View Article Online
DOI: 10.1039/D6SC03512D

Open Access Article. Published on 22 June 2026. Downloaded on 6/23/2026 5:02:46 AM.
This article is licensed under a Creative Commons Attribution-NonCommercial 3.0 Unported Licence.

Consistent with the solvation trends discussed above, MD simulations of self-diffusion coefficients (Figure 1d) reveal pronounced differences in ion transport behavior across the electrolyte systems. The self-diffusion coefficients were extracted from mean-square displacement (MSD) analyses (Figure S9-S13). Electrolytes containing cyclic fluorinated additives exhibit significantly reduced Li^+ diffusion coefficients (FEC + REF: 1.4×10^{-7} cm² s⁻¹; DFEC + REF: 1.1×10^{-7} cm² s⁻¹) compared to the reference electrolyte (2.7×10^{-7} cm² s⁻¹), reflecting stronger Li^+–solvent coordination and a more constrained, yet controlled, transport environment. In contrast, electrolytes incorporating linear fluorinated additives display more variable Li^+ diffusion (1.9–2.7 $\times 10^{-7}$ cm² s⁻¹), accompanied by relatively higher PF_6^- diffusion coefficients, indicative of weaker solvation structures and increased anion mobility [28]. To contextualize these simulation results experimentally, the bulk viscosity of each electrolyte was measured rheo meter (Figure S14). Viscosity increases monotonically from 2.5 cP (REF) to 2.9 cP (FEC and DFEC) and reaches 3.4–3.6 cP for the most fluorinated linear systems (TFDEC and TTFDEC). Despite this trend, Li^+ diffusion in the TFDEC and TTFDEC electrolytes remains comparable to or exceeds that of the reference, demonstrating a clear decoupling between bulk viscosity and Li^+ mobility that can only be rationalized by differences in local solvation coordination rather than macroscopic rheological properties. These trends are further corroborated by the calculated ion transference numbers.

As shown in Figure 1e, cyclic fluorinated additives yield the highest Li^+ transference numbers (FEC + REF: 0.42; DFEC + REF: 0.44), substantially exceeding that of the reference electrolyte (0.33). By contrast, linear fluorinated additives exhibit lower Li^+ transference numbers in the range of 0.31–0.37, consistent with diminished Li^+ binding and enhanced anion transport. The elevated Li^+ transference numbers associated with cyclic additives signify more efficient Li^+ transport, which is advantageous for high-rate operation by suppressing concentration polarization and

Chemical Science Accepted Manuscript

View Article Online
DOI: 10.1039/D6SC03512D

Open Access Article. Published on 22 June 2026. Downloaded on 6/23/2026 5:02:46 AM.
This article is licensed under a Creative Commons Attribution-NonCommercial 3.0 Unported Licence.

promoting a more uniform Li^+ flux across the electrode–electrolyte interface [29]. Independent experimental validation of the MD-derived diffusion coefficients was obtained by ^7Li DOSY NMR measurements (Figure S15). The DOSY-derived Li^+ diffusion coefficients are in good quantitative agreement with the MD simulations, confirming that cyclic FEC and DFEC most strongly suppress Li^+ mobility through tight solvation coordination, while TFDEC and TTFDEC allow near-reference Li^+ diffusion rates consistent with their exclusion from the primary coordination shell. This viscosity–diffusion decoupling, captured simultaneously by MD, rheology, and DOSY NMR, establishes that the transport behavior of these electrolytes is governed by solvation structure rather than bulk fluid properties.

In addition to these electronic and transport descriptors, we further quantified the steric footprint of each molecule using topographic steric maps and the corresponding buried volume $V_{\text{buried}}^{\text{CS}}$ (Figure 1f). The steric maps project the three-dimensional van der Waals envelope of each carbonate onto a 2D cross-section around the carbonyl coordination site, where the thickness of the red annulus reflects the local steric height. Cyclic carbonates (EC, FEC, DFEC) display compact, nearly circular steric profiles with identical $V_{\text{buried}}^{\text{CS}}$ values of 12.8 Å³, indicating that fluorination of the EC ring only weakly perturbs the steric accessibility of the carbonyl oxygen. By contrast, the linear DEC-based series exhibits substantially larger buried volumes: DEC, FDEC, and DFDEC already occupy 29.6–29.7 Å³, more than twice the steric volume of the cyclic analogues, while TFDEC further expands to 34.6 Å³. Notably, TTFDEC returns to 29.7 Å³—comparable to the mono- and difluorinated linear analogues—suggesting that the additional fluorine substituents in TTFDEC do not further increase steric bulk beyond that of DFDEC, and that steric hindrance alone cannot fully account for the near-complete solvation exclusion of TTFDEC. This implies that the exclusion of TTFDEC is driven predominantly by its severely

Chemical Science Accepted Manuscript

View Article Online
DOI: 10.1039/D6SC03512D

weakened carbonyl electron density and near-zero Li^+–solvent binding energy (−0.25 eV), rather than by geometric obstruction. TFDEC, in contrast, combines both an enlarged buried volume (34.6 Å³) and substantially weakened binding (−0.33 eV), making it the system where steric and electronic penalties act synergistically to produce solvation exclusion. When combined with the reduced carbonyl electron density and weakened binding energies discussed above, the large $V_{\text{buried}}^{\text{CS}}$ values and near-zero Li^+–additive coordination of TFDEC and TTFDEC together establish a dual steric–electronic origin for their solvation exclusion: these highly fluorinated linear additives are expelled from the Li^+ first solvation shell through distinct but reinforcing molecular mechanisms.

Open Access Article. Published on 22 June 2026. Downloaded on 6/23/2026 5:02:46 AM.
This article is licensed under a Creative Commons Attribution-NonCommercial 3.0 Unported Licence.

Chemical Science Accepted Manuscript

View Article Online
DOI: 10.1039/D6SC03512D

Open Access Article. Published on 22 June 2026. Downloaded on 6/23/2026 5:02:46 AM.
This article is licensed under a Creative Commons Attribution-NonCommercial 3.0 Unported Licence.

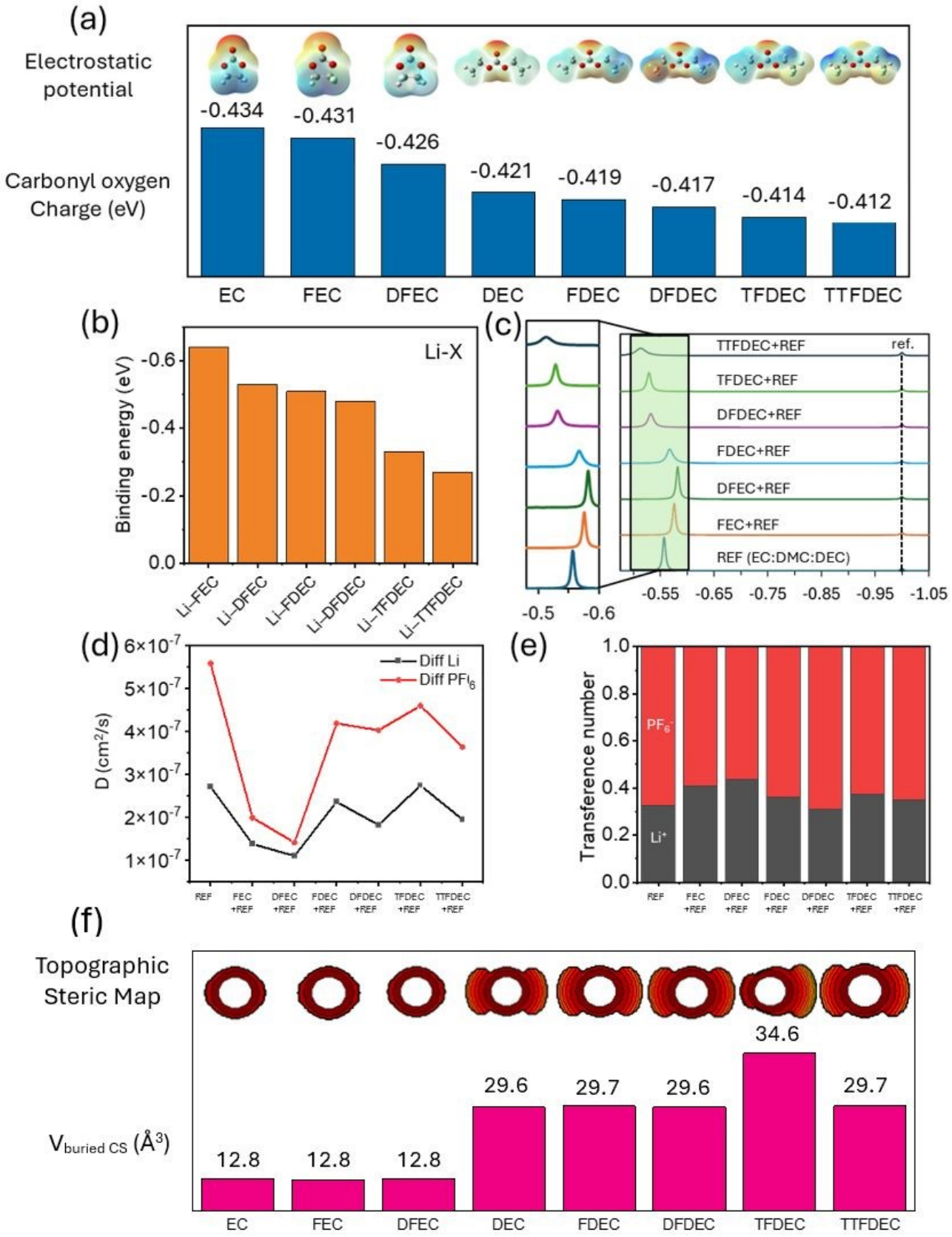

Figure 1. Fluorination-dependent Li^+ solvation and transport characteristics. (a) Electrostatic

Chemical Science Accepted Manuscript

View Article Online
DOI: 10.1039/D6SC03512D

Open Access Article. Published on 22 June 2026. Downloaded on 6/23/2026 5:02:46 AM.
This article is licensed under a Creative Commons Attribution-NonCommercial 3.0 Unported Licence.

potential maps and carbonyl oxygen partial charges of carbonate solvents and fluorinated additives. (b) DFT-calculated Li^+–solvent binding energies. (c) ^7Li NMR spectra of electrolytes with different fluorinated additives. (d) MD-derived self-diffusion coefficients of Li^+ and PF_6^-. (e) Corresponding Li^+ and PF_6^- transference numbers. (f) Topographic steric maps and corresponding buried volume

3.2 Solvation Exclusion in Highly Fluorinated Linear Carbonates Revealed by MD Simulations

To directly visualize and quantify fluorination-dependent solvation behavior, MD simulations were performed for all electrolyte formulations. Figure 2a and 2b present schematic representations of the two contrasting solvation regimes identified in this study. In the active solvation regime exemplified by FDEC (Figure 2a), the fluorinated additive occupies a bonafide coordination site within the Li^+ first solvation shell at a Li^+–O distance of ~2.3 Å, comparable to the coordination distances of EC, DEC, and DMC. The Li^+–FDEC coordination number of 0.59 ± 0.04 confirms that FDEC participates actively and reproducibly in the primary solvation shell alongside conventional carbonate solvents, with PF_6^- contributing only minimally (CN ~0.3). In stark contrast, the inactive solvation (solvation exclusion) regime in the TTFDEC-containing electrolyte (Figure 2b) shows that TTFDEC is pushed to the outer periphery of the solvation environment, residing at an average Li^+–O distance of 3.84 Å—well beyond the primary coordination sphere—and contributing a Li^+–TTFDEC coordination number of only 0.004 ± 0.001, corresponding to less than ~1% additive participation. The vacant coordination site vacated by TTFDEC is instead filled by DEC and DMC, whose CN rises 0.3-0.5. These schematics thus

Chemical Science Accepted Manuscript

View Article Online
DOI: 10.1039/D6SC03512D

Open Access Article. Published on 22 June 2026. Downloaded on 6/23/2026 5:02:46 AM.
This article is licensed under a Creative Commons Attribution-NonCommercial 3.0 Unported Licence.

define the two mechanistically distinct outcomes of fluorination: controlled coordination modulation versus effective self-exclusion from the solvation shell.

Importantly, this solvation exclusion mechanism is expected to hold fundamentally regardless of the specific lithium salt anion employed (e.g., PF_6^- vs. FSI^-, $TFSI^-$, or BF_4^-). Because the exclusion is driven primarily by extreme solvent–solvent thermodynamic competition and steric hindrance (Table 2 and Figure 1f), highly fluorinated linear carbonates lack the intrinsic Lewis basicity to displace conventional carbonates like EC or DMC. Consequently, whether paired with strongly coordinating anions that limit available solvation sites (promoting faster exclusion) or weakly coordinating anions that leave the shell solvent-dominated, molecules like TFDEC and TTFDEC are thermodynamically destined to reside outside the primary Li^+ coordination sphere in conventional multi-solvent systems [5].

The quantitative basis for these two regimes is provided by the radial coordination number profiles shown in Figure 2c and 2d. In the FDEC electrolyte (Figure 2c), the cumulative coordination number curves rise in a well-defined stepwise fashion, with Li^+–EC reaching ~3.0 at ~2.5 Å, Li^+–DEC ~1.5 at ~3.0 Å, Li^+–DMC ~0.6, and Li^+–FDEC plateauing at ~0.6 within the first coordination shell, confirming that all four species co-occupy the primary shell. The Li^+–PF_6^- profile rises more gradually, indicating predominantly outer-shell ion pairing. By contrast, in the TTFDEC electrolyte (Figure 2d), the Li^+–TTFDEC coordination curve remains flat and near-zero throughout the entire distance range up to 5 Å, while Li^+–DMC rises to ~1.1 to compensate. The profiles for Li^+–EC, Li^+–DEC, and Li^+–PF_6^- remain essentially unchanged between the two systems, confirming that solvation exclusion is specific to TTFDEC and does not globally disrupt the base carbonate solvation structure. Analysis based on the simulation box (Figure S16) and

Chemical Science Accepted Manuscript

View Article Online
DOI: 10.1039/D6SC03512D

complementary coordination snapshots (Figure S17, S18) further validate these trends across all fluorinated additives.

Figure 2e summarizes the Li^+ coordination numbers with each electrolyte component across all formulations, providing a quantitative overview of how fluorination degree reshapes the primary solvation shell. The contributions from EC and DEC remain nearly invariant across the series (Li^+–EC: 2.716–3.286; Li^+–DEC: 1.477–1.693), confirming that the base carbonate scaffold is not disrupted by additive substitution. The Li^+–DMC coordination, however, shows a compensatory increase as additive coordination diminishes: from 0.768 in FDEC to 1.055 in TFDEC, reflecting the progressive back-filling of the vacated additive coordination site by DMC as fluorination increases. The additive coordination number (Li-Add) drops precipitously from 0.697 (FEC) to 0.586 (FDEC), 0.183 (DFEC), 0.115 (DFDEC), 0.037 (TFDEC), and effectively zero for

Open Access Article. Published on 22 June 2026. Downloaded on 6/23/2026 5:02:46 AM.
This article is licensed under a Creative Commons Attribution-NonCommercial 3.0 Unported Licence.

Chemical Science Accepted Manuscript

View Article Online
DOI: 10.1039/D6SC03512D

TTFDEC, delineating a clear fluorination threshold beyond which the additive can no longer compete for the Li^+ first coordination sphere.

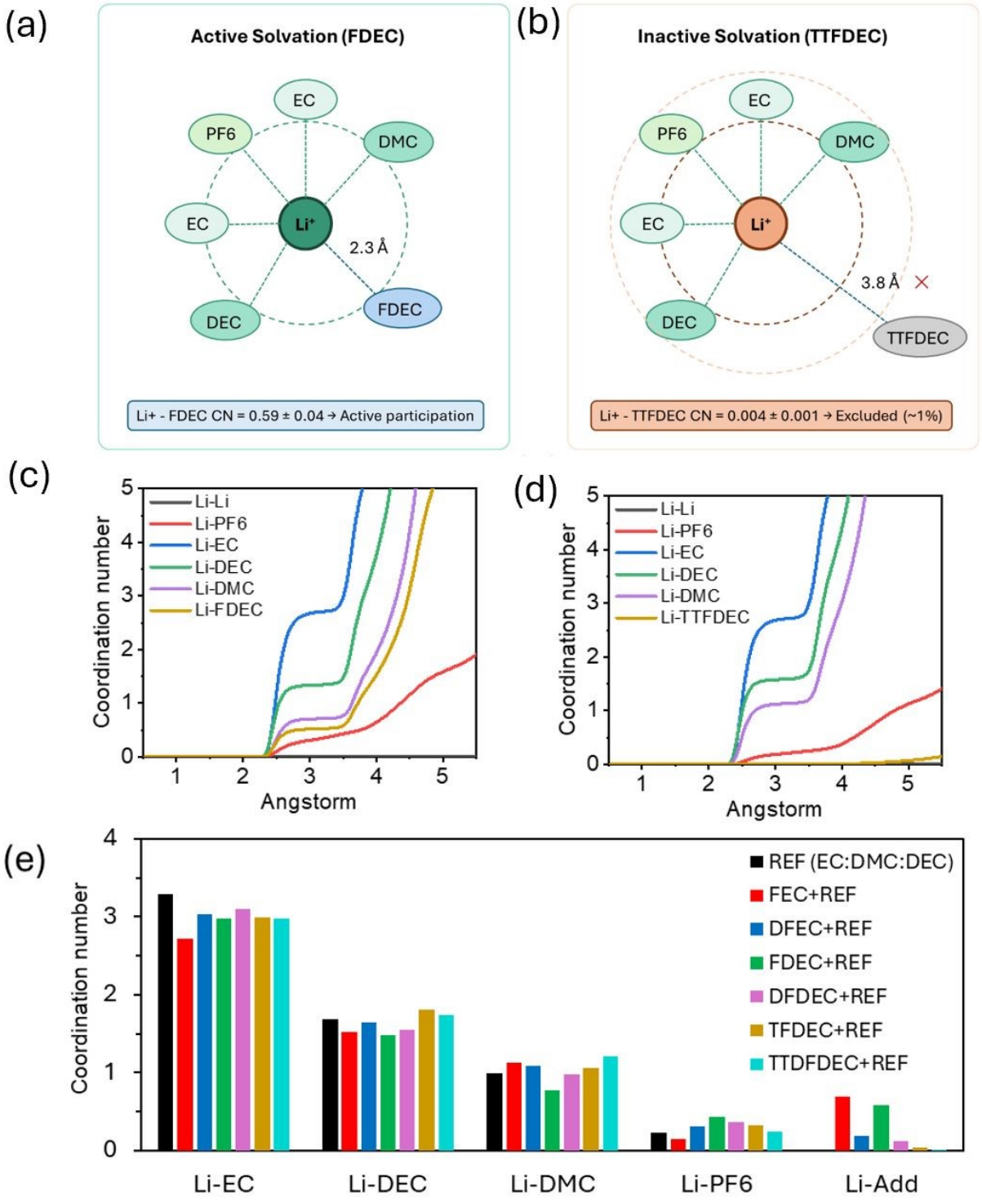

Open Access Article. Published on 22 June 2026. Downloaded on 6/23/2026 5:02:46 AM.
This article is licensed under a Creative Commons Attribution-NonCommercial 3.0 Unported Licence.

Chemical Science Accepted Manuscript

View Article Online
DOI: 10.1039/D6SC03512D

Open Access Article. Published on 22 June 2026. Downloaded on 6/23/2026 5:02:46 AM.
This article is licensed under a Creative Commons Attribution-NonCommercial 3.0 Unported Licence.

Figure 2. MD analysis of Li^+ solvation structures in electrolytes containing linear fluorinated carbonate additives. (a) Schematic representations of the Li^+ first solvation shell in FDEC- and (b) TTFDEC-containing electrolytes, illustrating active coordination of FDEC and complete exclusion of TTFDEC from the primary solvation shell. (c) Radial coordination number profiles of Li^+ with all electrolyte components as a function of Li–X distance (Å) in FDEC- and (d) TTFDEC-containing electrolytes. (e) Total coordination numbers of Li^+ with EC, DEC, DMC, PF_6^-, and fluorinated additives for all electrolyte formulations, extracted from MD simulations.

The complementary thermodynamic and ion-pairing analysis is presented in Table 1. The statistical significance of these reported coordination numbers is strongly supported by the deep equilibration of the system, as evidenced by the block average standard error profiles (Figure S4). This rigorous statistical independence validates that the time-averaged structural properties derived from the final 4 ns production window are highly representative of the bulk behavior. The reference electrolyte exhibits a low Li^+–PF_6^- coordination number (0.228) and CIP fraction of 3.67% ($\Delta_r G_{CIP}$ = 1.933 kcal mol^{-1}), establishing the baseline for a solvent-dominated solvation environment. In the cyclic series, FEC and DFEC systematically increase Li^+–PF_6^- coordination (0.250 and 0.317) and CIP fraction (3.95% and 5.07%) while lowering $\Delta_r G_{CIP}$ to 1.889 and 1.734 kcal mol^{-1}, respectively, consistent with active additive participation promoting controlled contact ion-pair formation favorable for LiF-rich SEI generation [30]. In the linear series, a non-monotonic trend emerges. FDEC achieves the highest Li^+–PF_6^- coordination (0.431) and CIP fraction (6.90%) with the lowest $\Delta_r G_{CIP}$ (1.540 kcal mol^{-1}) of any system, reflecting a synergistic combination of active additive coordination (CN = 0.586) and electrostatic modulation. With increasing fluorination, however, both Li^+–PF_6^- coordination and CIP fraction decline

Chemical Science Accepted Manuscript

View Article Online
DOI: 10.1039/D6SC03512D

Open Access Article. Published on 22 June 2026. Downloaded on 6/23/2026 5:02:46 AM.
This article is licensed under a Creative Commons Attribution-NonCommercial 3.0 Unported Licence.

progressively through DFDEC (0.361, 5.91%) and TFDEC (0.321, 5.16%), as the additives are increasingly excluded from the solvation shell. At the extreme, TFDEC and TTFDEC contribute negligible additive coordination (0.037 and ~0.004), and the solvation structure reverts toward the reference baseline. Li^+ thus becomes confined in a rigid, carbonate-dominated shell with limited PF_6^- accessibility—a kinetically trapped configuration that manifests as elevated charge-transfer resistance and poor cycling stability in subsequent sections. These results establish that mono-fluorinated FDEC represents the optimal linear additive, simultaneously maximizing coordination, CIP formation, and ion-pair thermodynamics [31].

Table 1. The coordination number, Contact/Separated Ion Pair Distributions and corresponding contact ion pair formation energy (kcal mol-1) attributed to each molecule present in the first solvation shell of the electrolyte system, as observed using molecular dynamics simulation.

Systems	Li^+-Li^+	Li^+-PF_6^-	Li^+-EC	Li^+-DEC	Li^+-DMC	Li^+-Additives	%CIP	%SSIP	$\Delta_f G_{CIP}$
REF (1M $LiPF_6$ EC: DEC: DMC)	0.00	0.228	3.286	1.693	0.99	-	3.67	96.33	1.933
FEC+REF	0.00	0.25	2.716	1.528	1.131	0.697	3.95	96.05	1.889
DFEC+REF	0.00	0.317	3.03	1.639	1.082	0.183	5.07	94.93	1.734
FDEC+REF	0.00	0.431	2.977	1.477	0.768	0.586	6.90	93.10	1.540
DFDEC+REF	0.00	0.361	3.096	1.544	0.985	0.115	5.91	94.09	1.638
TFDEC+REF	0.00	0.321	2.996	1.803	1.055	0.037	5.16	94.84	1.722
TTFDEC+REF	0.00	0.25	2.985	1.745	1.206	0.004	4.03	95.97	1.875

Chemical Science Accepted Manuscript

View Article Online
DOI: 10.1039/D6SC03512D

Open Access Article. Published on 22 June 2026. Downloaded on 6/23/2026 5:02:46 AM.
This article is licensed under a Creative Commons Attribution-NonCommercial 3.0 Unported Licence.

To account for competitive coordination in the full electrolyte environment, we performed cluster-DFT desolvation energy calculations on representative first-solvation-shell snapshots extracted from MD trajectories—Li^+(2EC·DEC·DMC·PF_6^-·Additive)—rather than isolated Li^+–additive dimers. The cluster compositions in Table 2 reflect thermally equilibrated liquid-phase structures. The cluster desolvation energies reveal a striking bifurcation absent in single-molecule analysis. In the active solvation regime (REF, FEC, DFEC, FDEC, DFDEC), energies range from −72.41 to −184.51 kcal mol^{-1}, confirming thermodynamically stable Li^+ coordination despite competing solvents. Cyclic additives FEC (−179.54 kcal mol^{-1}) and DFEC (−184.51 kcal mol^{-1}) substantially deepen binding relative to REF (−90.19 kcal mol^{-1}), while linear FDEC (−72.41 kcal mol^{-1}) and DFDEC (−73.16 kcal mol^{-1}) remain thermodynamically favorable, consistent with their partial coordination numbers (0.586 and 0.115, respectively; Figure 2e). In stark contrast, the solvation exclusion regime emerges unambiguously for TFDEC and TTFDEC, whose cluster desolvation energies collapse to −1.36 and −3.21 kcal mol^{-1}—approaching the thermal energy scale (~0.59 kcal mol^{-1} at room temperature)—indicating near-zero thermodynamic gain from Li^+ coordination in the competitive environment, consistent with MD-derived coordination numbers of 0.037 and 0.004 (Table 1). This thermodynamic cliff between DFDEC and TFDEC is entirely absent in single-molecule binding energies, which show only a gradual decrease from FEC (−0.64 eV) to TTFDEC (−0.25 eV). Together, Table 2, Figure 2e, and Figure S17 and S18 establish that the active solvation vs. solvation exclusion distinction is governed by thermodynamic competition for Li^+ coordination sites, not by intrinsic Li^+–additive affinity alone.

The physical origin of this solvation exclusion threshold (e.g., CN < 0.04 for TFDEC and TTFDEC) is governed by a crossover of steric and thermodynamic penalties in the competitive electrolyte environment. As illustrated by the topographic steric maps (Figure 1f), highly

Chemical Science Accepted Manuscript

View Article Online
DOI: 10.1039/D6SC03512D

Open Access Article. Published on 22 June 2026. Downloaded on 6/23/2026 5:02:46 AM.
This article is licensed under a Creative Commons Attribution-NonCommercial 3.0 Unported Licence.

fluorinated linear carbonates possess a substantially enlarged buried volume (V_{buried}) of 34.6 Å³ for TFDEC compared to their cyclic analogues (12.8 Å³), introducing severe steric repulsion within the compact primary solvation shell. Furthermore, while the Natural Bond Orbital (NBO) charges on the carbonyl oxygen remain relatively invariant across the series (Figure S6), the strong through-space inductive effects of excessive fluorination drastically suppress the overall electrostatic interaction. Consequently, cluster-DFT desolvation energies (Table 2) reveal that the coordination of TFDEC and TTFDEC provides essentially no thermodynamic stabilization (-1.36 and -3.21 kcal mol^{-1}, respectively) when competing with conventional carbonates, driving their statistical exclusion from the Li^+ first solvation shell.

Table 2. Cluster Compositions and DFT-Calculated Desolvation Energies of Li^+ Solvation Shells Containing Fluorinated Carbonate Additives

Electrolyte System	Solvation Shell Composition	Desolvation Energy (kcal/mol)
REF (1M $LiPF_6$ EC:DEC:DMC)	Li^+-(2EC·DEC·DMC·PF_6^-)	−90.19
FEC+REF	Li^+-(2EC·DEC·DMC·PF_6^-·FEC)	−179.54
DFEC+REF	Li^+-(2EC·DEC·DMC·PF_6^-·DFEC)	−184.51
FDEC+REF	Li^+-(2EC·DEC·DMC·PF_6^-·FDEC)	−72.41
DFDEC+REF	Li^+-(2EC·DEC·DMC·PF_6^-·DFDEC)	−73.16
TFDEC+REF	Li^+-(2EC·DEC·DMC·PF_6^-·TFDEC)	−1.36
TTFDEC+REF	Li^+-(2EC·DEC·DMC·PF_6^-·TTFDEC)	-3.21

Chemical Science Accepted Manuscript

View Article Online
DOI: 10.1039/D6SC03512D

Open Access Article. Published on 22 June 2026. Downloaded on 6/23/2026 5:02:46 AM.
This article is licensed under a Creative Commons Attribution-NonCommercial 3.0 Unported Licence.

3.3 Electrochemical Manifestations of Active and Inactive Solvation During Formation and Cycling

Before presenting the electrochemical results, we clarify the experimental design rationale. NMC90 electrodes with active mass loadings of 31.6, 24.1, and 21.2 mg cm^{-2} were used for Figure 3a–e, 3f–g, and 3h–i, respectively; all electrodes were calendered to ~35% porosity with a standardized 12-hour wetting rest prior to formation. To decouple fluorination degree from concentration effects, Figure 3h–i present data at a fixed 25 vol% across all additives. At this fixed concentration, highly fluorinated linear additives (TFDEC, TTFDEC) cause catastrophic capacity loss during formation (Figure S19a), confirming that their poor performance is intrinsic to excessive fluorination rather than low additive quantity. This control justifies the inverse-scaled concentration design in Figure 3a–g, where concentrations were reduced for highly fluorinated additives solely to prevent irreversible cell failure and enable meaningful characterization of the fluorination effect itself. The paired design thus isolates the intrinsic molecular contribution of fluorination from any concentration-dependent artifact.

Oxidative stability was further assessed by potentiostatic voltage-holding experiments on NMC90||Li half-cells from 4.3 to 4.9 V vs. Li/Li^+ (Figure S20). The DFEC-based electrolyte exhibits the most favorable oxidative response, with rapidly decaying anodic currents at each potential step up to ~4.6 V and a clearly delayed decomposition onset relative to REF and all linear systems, consistent with formation of a compact, passivating CEI derived from solvation-shell-directed DFEC decomposition. FEC displays a similarly restrained profile, corroborating the effectiveness of cyclic fluorinated additives in cathode interphase protection. In contrast, TFDEC

Chemical Science Accepted Manuscript

View Article Online
DOI: 10.1039/D6SC03512D

Open Access Article. Published on 22 June 2026. Downloaded on 6/23/2026 5:02:46 AM.
This article is licensed under a Creative Commons Attribution-NonCommercial 3.0 Unported Licence.

and TTFDEC show substantially elevated, slowly decaying anodic currents from ~4.4 V onward, reflecting their inability to form a protective CEI and leaving the NMC90 surface continuously exposed to oxidative decomposition. FDEC and DFDEC display intermediate stability, consistent with their partial solvation participation. The resulting stability ranking — DFEC ≈ FEC > DFDEC ≈ FDEC > REF > TFDEC ≈ TTFDEC — mirrors precisely the hierarchy of capacity retention, ICE, and interphase quality across all other analyses, providing direct electrochemical confirmation that solvation-mediated CEI formation governs high-voltage oxidative stability in Ni-rich cathodes.

During the initial formation cycle at C/20 (Figure 3a), all electrolyte formulations deliver high initial charge capacities (averaged over three cells): REF (206.92 ± 0.45 mAh g^{-1}), FEC (207.64 ± 1.36 mAh g^{-1}), DFEC (199.53 ± 5.59 mAh g^{-1}), FDEC (191.23 ± 1.40 mAh g^{-1}), DFDEC (201.41 ± 2.57 mAh g^{-1}), TFDEC (186.79 ± 4.99 mAh g^{-1}), and TTFDEC (198.38 ± 4.15 mAh g^{-1}). Electrolytes containing cyclic fluorinated additives exhibit superior initial coulombic efficiencies (ICEs): FEC (85.80 ± 0.19%) and DFEC (84.01 ± 0.99%), both exceeding the reference electrolyte (84.04 ± 0.28%) and all linear analogues (Figure 3b). Mechanistically, the higher ICE of cyclic additives reflects their active participation in the Li^+ solvation shell (CN = 0.697 for FEC, 0.183 for DFEC), which facilitates preferential, early reductive decomposition of the fluorinated additive during the first lithiation. This produces a compact, LiF-rich SEI with low electronic conductivity that efficiently passivates the graphite surface and suppresses continued electrolyte decomposition. The irreversible capacity during formation is thus concentrated in a single, well-defined SEI formation event rather than spread over multiple cycles as parasitic reactions. This mechanistic picture is fully corroborated by the voltage-holding oxidative stability data (Figure S20): the same additives that direct reductive SEI formation at the anode during the

Chemical Science Accepted Manuscript

View Article Online
DOI: 10.1039/D6SC03512D

Open Access Article. Published on 22 June 2026. Downloaded on 6/23/2026 5:02:46 AM.
This article is licensed under a Creative Commons Attribution-NonCommercial 3.0 Unported Licence.

first lithiation also confer the most effective passivation against oxidative decomposition at the cathode, confirming that solvation-shell participation governs interphase quality simultaneously at both electrodes.

In contrast, linear fluorinated additives — particularly those with high fluorination degrees — display substantially lower ICEs: FDEC (80.56 ± 0.04%), DFDEC (80.98 ± 3.52%), TFDEC (73.90 ± 1.45%), and TTFDEC (78.02 ± 1.29%). The depressed ICE of highly fluorinated linear additives has a distinct mechanistic origin from that of cyclic systems. Because TFDEC and TTFDEC are largely excluded from the Li^+ solvation shell (CN = 0.037 and 0.004, respectively), these molecules do not participate in the directed SEI formation pathway that cyclic additives enable. Instead, the conventionally solvated Li^+ (EC- and DMC-dominated shell) undergoes reductive decomposition via standard carbonate pathways, generating a thicker, organically rich, and less uniform interphase. The higher irreversible capacity in these systems thus reflects not additive-mediated SEI formation, but continued parasitic carbonate reduction across multiple formation cycles, consistent with the higher $\Delta_r G_{CIP}$ values and weaker ion-pairing thermodynamics observed in Table 1. The elevated and poorly passivating anodic currents observed for TFDEC and TTFDEC in the voltage-holding test (Figure S20) provide direct electrochemical confirmation of this picture: solvation exclusion prevents the formation of a protective CEI at the cathode, just as it prevents directed SEI formation at the anode, resulting in continuous parasitic electrolyte decomposition at both electrodes during the formation process.

When cycled at C/10 (Figure 3c), the discharge capacities stabilize at: REF (193.68 ± 0.22 mAh g^{-1}), FEC (194.86 ± 2.12 mAh g^{-1}), DFEC (190.61 ± 5.63 mAh g^{-1}), FDEC (183.89 ± 0.16 mAh g^{-1}), DFDEC (190.91 ± 2.26 mAh g^{-1}), TFDEC (176.60 ± 2.20 mAh g^{-1}), and TTFDEC (187.75 ± 3.73 mAh g^{-1}). Cells employing moderately fluorinated cyclic additives (FEC, DFEC) and

Chemical Science Accepted Manuscript

View Article Online
DOI: 10.1039/D6SC03512D

Open Access Article. Published on 22 June 2026. Downloaded on 6/23/2026 5:02:46 AM.
This article is licensed under a Creative Commons Attribution-NonCommercial 3.0 Unported Licence.

mono-fluorinated linear FDEC retain higher capacities and improved cycling stability. The GCD profiles (Figure 3c) further show that FEC- and DFEC-based electrolytes exhibit reduced voltage polarization at C/10, consistent with lower interfacial impedance. Differential capacity (dQ/dV) analysis (Figure S21) reveals that cyclic fluorinated electrolytes display sharper and more symmetric phase-transition peaks for the graphite staging reactions, indicating improved Li^+ intercalation kinetics and more reversible lithium utilization enabled by the higher-quality SEI formed during the initial cycles. Collectively, the convergent evidence from ICE analysis, GCD profiles, dQ/dV features, and voltage-holding oxidative stability tests establishes a self-consistent picture in which the degree of additive incorporation into the Li^+ solvation shell is the single decisive variable governing electrochemical performance: solvation-active additives (DFEC, FEC) simultaneously minimize irreversible capacity loss during formation, suppress cathodic voltage polarization during cycling, and confer high-voltage oxidative stability at the cathode, whereas solvation-inactive additives (TFDEC, TTFDEC) fail on all three metrics in direct proportion to their exclusion from the Li^+ coordination environment.

Rate performance was evaluated by stepwise increasing current density from C/10 to 1.5C, followed by recovery at C/10 (Figure 3d). Cells containing highly fluorinated linear additives suffer severe capacity loss at high rates, delivering only 25.01 mAh g^{-1} (TFDEC) and 19.11 mAh g^{-1} (TTFDEC) at 1.5C. This dramatic rate failure is mechanistically linked to solvation exclusion: because TFDEC and TTFDEC do not modulate the Li^+ desolvation barrier at the electrode–electrolyte interface, charge-transfer kinetics remain dominated by the high-barrier EC-solvated Li^+ shell, leading to severe concentration polarization under high-current conditions—a penalty that is amplified by the relatively thick electrodes (31.6 mg cm^{-2}) used in this series. Lower-fluorinated linear additives (FDEC: 73.04 mAh g^{-1}; DFDEC: 74.09 mAh g^{-1}) significantly

Chemical Science Accepted Manuscript

View Article Online
DOI: 10.1039/D6SC03512D

Open Access Article. Published on 22 June 2026. Downloaded on 6/23/2026 5:02:46 AM.
This article is licensed under a Creative Commons Attribution-NonCommercial 3.0 Unported Licence.

outperform both DFEC (59.45 mAh g^{-1}) and the reference (46.19 mAh g^{-1}) at 1.5C, while FEC delivers the highest high-rate capacity of 90.81 mAh g^{-1}. The extended rate capability to 5C (Figure 3f, 24.1 mg cm^{-2}) further reinforces this ranking, with FEC and DFEC maintaining meaningful capacity at extreme rates while TFDEC- and TTFDEC-based cells collapse. Both FEC and DFEC also exhibit excellent capacity recovery upon return to C/10 (178.17 and 169.43 mAh g^{-1}, respectively), confirming that the kinetic advantages of active solvation are fully reversible. Comparable trends are confirmed in cathode and anode half-cell measurements (Figure S22 and S23).

Long-term cycling stability was assessed between 3.0–4.2 V at C/2 for 500 cycles (Figure 3e). Among the scaled-concentration series, DFEC-based cells achieve the highest final discharge capacity (97.54 mAh g^{-1}) with 81.90% retention, followed by FEC (92.59 mAh g^{-1}, 68.45%), FDEC (88.42 mAh g^{-1}, 69.10%), and the reference (86.99 mAh g^{-1}, 76.90%). DFDEC shows inferior retention (68.70 mAh g^{-1}, 49.74%), while TFDEC and TTFDEC suffer catastrophic degradation, retaining only 8.09 mAh g^{-1} (13.21%) and 32.92 mAh g^{-1} (36.22%), respectively. To confirm that this degradation hierarchy is a property of fluorination degree rather than additive concentration, the fixed-concentration control experiment (25 vol% for all, Figure 3h–i, 21.2 mg cm^{-2}) reproduces the same ranking with even more pronounced differentiation: TFDEC and TTFDEC cells fail during formation or within the first 50 cycles, while FEC and DFEC maintain >80% retention at 200 cycles. The thinner electrodes (21.2 mg cm^{-2}) in this series rule out mass-transport limitations as a confounding variable, confirming that the observed performance differences originate from electrolyte–electrode interfacial chemistry rather than electrode engineering parameters.

Chemical Science Accepted Manuscript

View Article Online
DOI: 10.1039/D6SC03512D

Open Access Article. Published on 22 June 2026. Downloaded on 6/23/2026 5:02:46 AM.
This article is licensed under a Creative Commons Attribution-NonCommercial 3.0 Unported Licence.

Under the elevated cut-off voltage of 4.5 V at 2C for 200 cycles (Figure 3g, 24.1 mg cm^{-2}), the performance hierarchy shifts relative to the low-rate cycling results, consistent with the rate capability data in Figure 3d and 3f. FDEC-based cells remarkably achieve ~100% retention at ~50 cycles before stabilizing above 80%, outperforming both FEC and REF maintain ~60% retention, which reflects the superior high-rate Li^+ desolvation kinetics of mono-fluorinated linear carbonate already demonstrated in the rate capability tests. DFEC retain ~40–50%, despite its excellent performance at moderate rates and low-rate long-term cycling (Figure 3e), shows comparatively lower retention at 2C—a behavior consistent with the lower high-rate capacities observed for DFEC in Figure 3d (59.45 mAh g^{-1} at 1.5C vs. 73.04 mAh g^{-1} for FDEC), suggesting that the rigid cyclic framework of DFEC, while advantageous for SEI quality, introduces a kinetic penalty at elevated current densities. FEC and REF retain intermediate performance at 2C/4.5 V, while TFDEC- and TTFDEC-based cells show rapid decay, further confirming that solvation exclusion translates directly to kinetic failure under demanding cycling conditions. These results establish that the performance ranking at high C-rates (FDEC > FEC > REF > DFEC) and at low C-rates (DFEC > FEC ≈ FDEC > REF) reflect two complementary aspects of the active solvation mechanism: optimized desolvation kinetics for rate performance versus stable, fluorine-rich interphase formation for long-term retention.

To further bridge the gap between fundamental solvation behavior and practical application, the electrochemical protocols designed in this work closely emulate practically relevant engineering scenarios. Specifically, addressing the critical demand of the electric vehicle (EV) industry for extreme fast charging, the robust high-rate capability sustained up to 5C (equivalent to a full charge in approximately 12 minutes) (Figure 3f) and the demanding long-term cycling protocol at an elevated current density of 2C under a high cut-off voltage of 4.5 V (Figure 3g) represent realistic

Chemical Science Accepted Manuscript

View Article Online
DOI: 10.1039/D6SC03512D

Open Access Article. Published on 22 June 2026. Downloaded on 6/23/2026 5:02:46 AM.
This article is licensed under a Creative Commons Attribution-NonCommercial 3.0 Unported Licence.

fast-charging and high-energy-density cell conditions. Furthermore, the fixed-concentration control series (25 vol%, Figure 3h–i) successfully isolates the chemical and interfacial stability of the electrolyte components under extreme local concentrations, confirming that the observed kinetic advantages or degradation patterns are intrinsic to the molecular structures of the additives rather than mere volumetric artifacts.

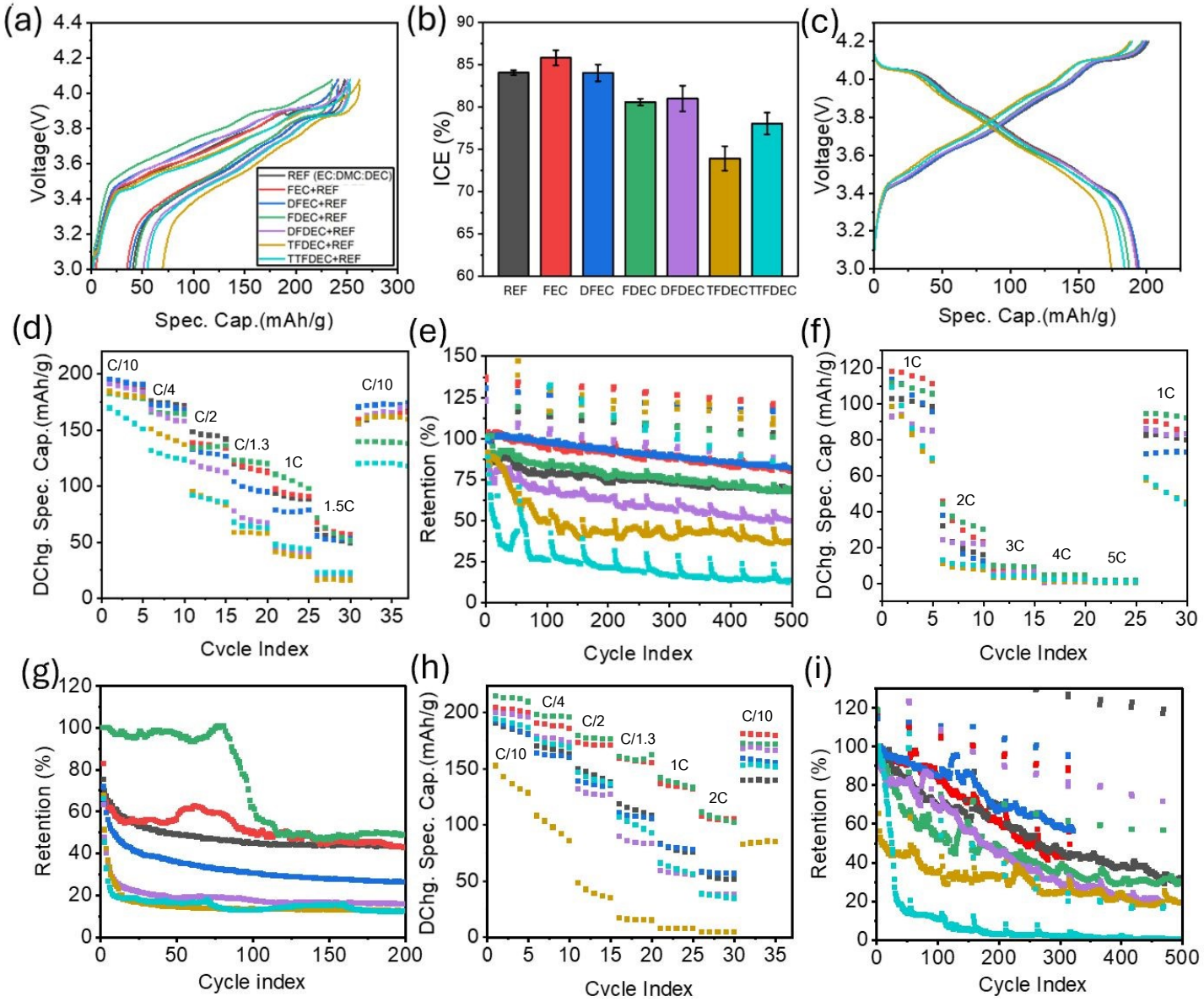

Chemical Science Accepted Manuscript

View Article Online
DOI: 10.1039/D6SC03512D

Open Access Article. Published on 22 June 2026. Downloaded on 6/23/2026 5:02:46 AM.
This article is licensed under a Creative Commons Attribution-NonCommercial 3.0 Unported Licence.

Figure 3. Electrochemical performance of NMC90‖graphite full cells with fluorinated electrolyte additives (a) Initial charge–discharge voltage profiles at C/20. (b) Initial Coulombic efficiency (ICE) comparison across all formulations with error bars from average 3 cells. (c) Galvanostatic charge–discharge (GCD) profiles at C/10. (d) Rate capability from C/10 to 1.5C (scaled additive concentration series). (e) Long-term capacity retention (%) over 500 cycles at C/2. (f) Rate capability from 1C to 5C (scaled additive concentration series). (g) Long-term capacity retention (%) over 200 cycles at 2C under cut-off voltage (4.5 V). (h) Rate capability from C/10 to 2C under fixed 25 vol% concentration for all fluorinated additives. (i) Long-term capacity retention (%) over 500 cycles at C/2 under fixed 25 vol% additive concentration for all fluorinated additives.

3.4 Bulk Diffusion versus Interfacial Control: Insights from GITT Analysis

Figure 4a presents the galvanostatic intermittent titration technique (GITT) voltage profiles of NMC90 cathodes during the first charge–discharge cycle for all electrolyte formulations. The characteristic saw-tooth features originate from alternating current pulses and relaxation periods, and the amplitude of the voltage oscillations directly reflects the magnitude of the overpotential, providing a qualitative measure of interfacial charge-transfer kinetics and transport limitations. Electrolytes containing cyclic fluorinated additives (FEC and DFEC) exhibit the smallest voltage oscillations, indicating reduced overpotential and more facile interfacial charge transfer compared to linear and highly fluorinated counterparts. The GITT-derived lithium-ion diffusion coefficients during charge and discharge (Figure 4b, c) further indicate that electrolyte composition has only a limited effect on solid-state Li^+ diffusion within the NMC90 cathode. Across all formulations, D_{Li^+} values remain within a narrow range of 2.0–4.5 × 10^{-12} cm^2 s^{-1}, a variation that is substantially

Chemical Science Accepted Manuscript

View Article Online
DOI: 10.1039/D6SC03512D

smaller than the 6–14-fold enhancement reported when comparing single-crystal and polycrystalline NMC cathodes [34]. This weak dependence on electrolyte chemistry is expected, as Li^+ transport within NMC90 is primarily governed by intrinsic factors such as crystal structure, lithiation state, and particle morphology. In contrast, electrolyte modifications mainly affect interfacial charge-transfer resistance and the properties of the SEI/CEI, rather than intraparticle diffusion kinetics [35]. Consequently, the superior electrochemical performance observed for FEC- and DFEC-based electrolytes (Figure 3d–i) can be attributed predominantly to enhanced interfacial kinetics and the formation of a stable, low-resistance interphase. This interpretation is further supported by their reduced charge-transfer activation energies (Figure 8) and higher Li^+

Open Access Article. Published on 22 June 2026. Downloaded on 6/23/2026 5:02:46 AM.
This article is licensed under a Creative Commons Attribution-NonCommercial 3.0 Unported Licence.

Chemical Science Accepted Manuscript

View Article Online
DOI: 10.1039/D6SC03512D

Open Access Article. Published on 22 June 2026. Downloaded on 6/23/2026 5:02:46 AM.
This article is licensed under a Creative Commons Attribution-NonCommercial 3.0 Unported Licence.

transference numbers (Figure 1e), rather than by any substantial improvement in bulk Li^+ diffusion within the cathode.

Figure 4. Lithium-ion transport behavior in NMC90 cathodes with different fluorinated electrolyte formulations. (a) Voltage profiles during the first charge–discharge cycle measured by the GITT. (b) Lithium-ion diffusion coefficients (D_{Li}^+) derived from GITT during the charge process. (c) D_{Li}^+ derived from GITT during the discharge process.

3.5 Structural Degradation Driven by Electrolyte Solvation Chemistry

FESEM images after 500 cycles (Figure 5) demonstrate that solvation structure governs cathode

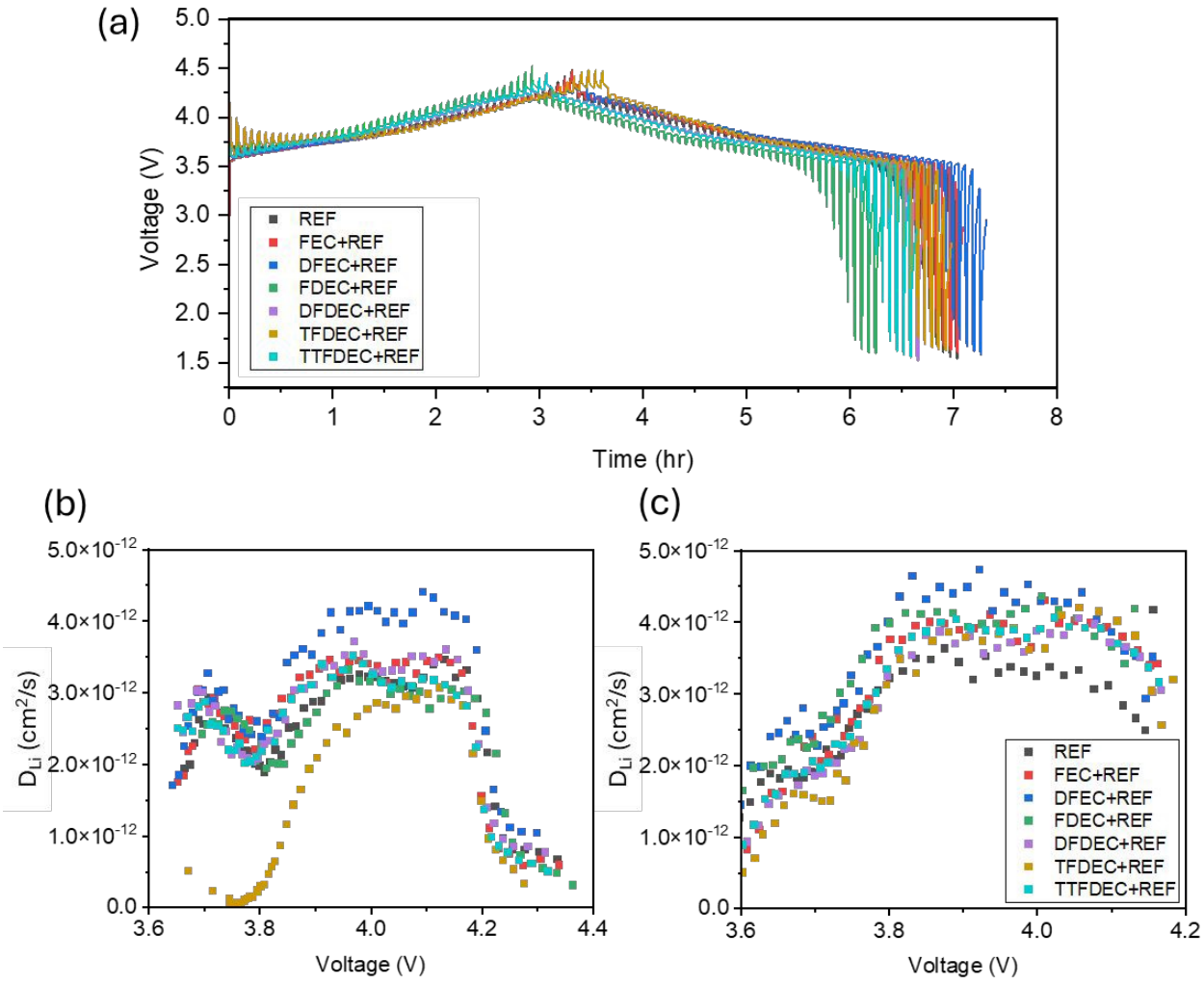

degradation across multiple length scales. The reference electrolyte (Figure 5a) shows moderate

Chemical Science Accepted Manuscript

View Article Online
DOI: 10.1039/D6SC03512D

Open Access Article. Published on 22 June 2026. Downloaded on 6/23/2026 5:02:46 AM.
This article is licensed under a Creative Commons Attribution-NonCommercial 3.0 Unported Licence.

surface roughening and limited intergranular microcracking on secondary particles, with mildly undulating primary particle surfaces indicative of grain-boundary stress accumulation.

Cyclic fluorinated additives yield markedly superior morphological stability. FEC-based cells (Figure 5b) exhibit compact secondary particles with smooth outlines and flat primary surfaces, consistent with stable solvation-shell participation promoting protective interphase chemistry. DFEC-based cells (Figure 5c) similarly maintain well-preserved secondary spheres and smooth primary surfaces. Quantitative AFM on the DFEC-cycled cathode (Figure S24, Table S5) confirms this superiority: exceptionally low surface roughness (Sq = 0.0779 μm at 5 μm; 0.2073 μm at 10 μm), minimal area ratio (SDR = 7.11%), and negative skewness (SSK = −0.5752 at 5 μm) collectively indicate a dense, valley-dominated surface topography characteristic of a compact, uniform CEI formed through directed DFEC decomposition rather than uncontrolled carbonate reduction. Low RMS slope (SDQ = 0.4072 rad) and reduced peak height (SPK = 0.1214 μm) further confirm the absence of significant intergranular cracking or localized deposit accumulation. Moderately fluorinated linear additives (FDEC, DFDEC; Figure 5d–e) show intermediate behavior — largely preserved secondary morphology but increased primary particle surface undulation — suggesting less effective suppression of intergranular stress. Highly fluorinated linear additives (TFDEC, TTFDEC; Figure 5f–g) induce severe degradation: extensive intergranular cracking, partial secondary particle fragmentation, and pronounced primary particle surface roughening, fully consistent with their solvation exclusion, low CIP populations, elevated charge-transfer activation energies (Figure 8), and rapid electrochemical capacity fading.

Complementary FESEM of graphite anodes (Figure S25) reinforces these trends. The reference electrolyte produces a thick, heterogeneous SEI with aggregated deposits and blurred flake edges, reflecting continuous uncontrolled carbonate decomposition. The DFEC-based anode exhibits a

Chemical Science Accepted Manuscript

View Article Online
DOI: 10.1039/D6SC03512D

markedly thinner, more uniform SEI with clearly discernible graphite flakes and no particle exfoliation. AFM quantification confirms this quality: low roughness (Sq = 0.1534 μm at 5 μm), exceptionally small valley void volume (VVV = 3.98×10^{-9} ml/m²), and a skewness transition from slightly negative at 5 μm (SSK = −0.1116) to modestly positive at 10 μm (SSK = +0.4510), reflecting an SEI that is locally smooth and nanoscale-uniform yet conformally follows graphite step-edge topography at larger scales — a hallmark of directed, LiF-rich SEI formation through preferential DFEC reduction within the Li^+ solvation shell. FDEC and DFDEC anodes show intermediate morphologies with increased roughness and patchy deposits, while TFDEC and TTFDEC anodes develop heavily cracked, irregular SEI layers that obscure graphite texture entirely — a direct consequence of solvation exclusion forcing SEI formation through uncontrolled carbonate decomposition. The parallel degradation trends across both electrodes confirm that active solvation participation stabilizes interphases cell-wide, whereas solvation exclusion produces mechanically fragile, chemically unstable interfaces throughout the full cell.

Open Access Article. Published on 22 June 2026. Downloaded on 6/23/2026 5:02:46 AM.
This article is licensed under a Creative Commons Attribution-NonCommercial 3.0 Unported Licence.

Chemical Science Accepted Manuscript

View Article Online
DOI: 10.1039/D6SC03512D

Open Access Article. Published on 22 June 2026. Downloaded on 6/23/2026 5:02:46 AM.
This article is licensed under a Creative Commons Attribution-NonCommercial 3.0 Unported Licence.

Chemical Science Accepted Manuscript

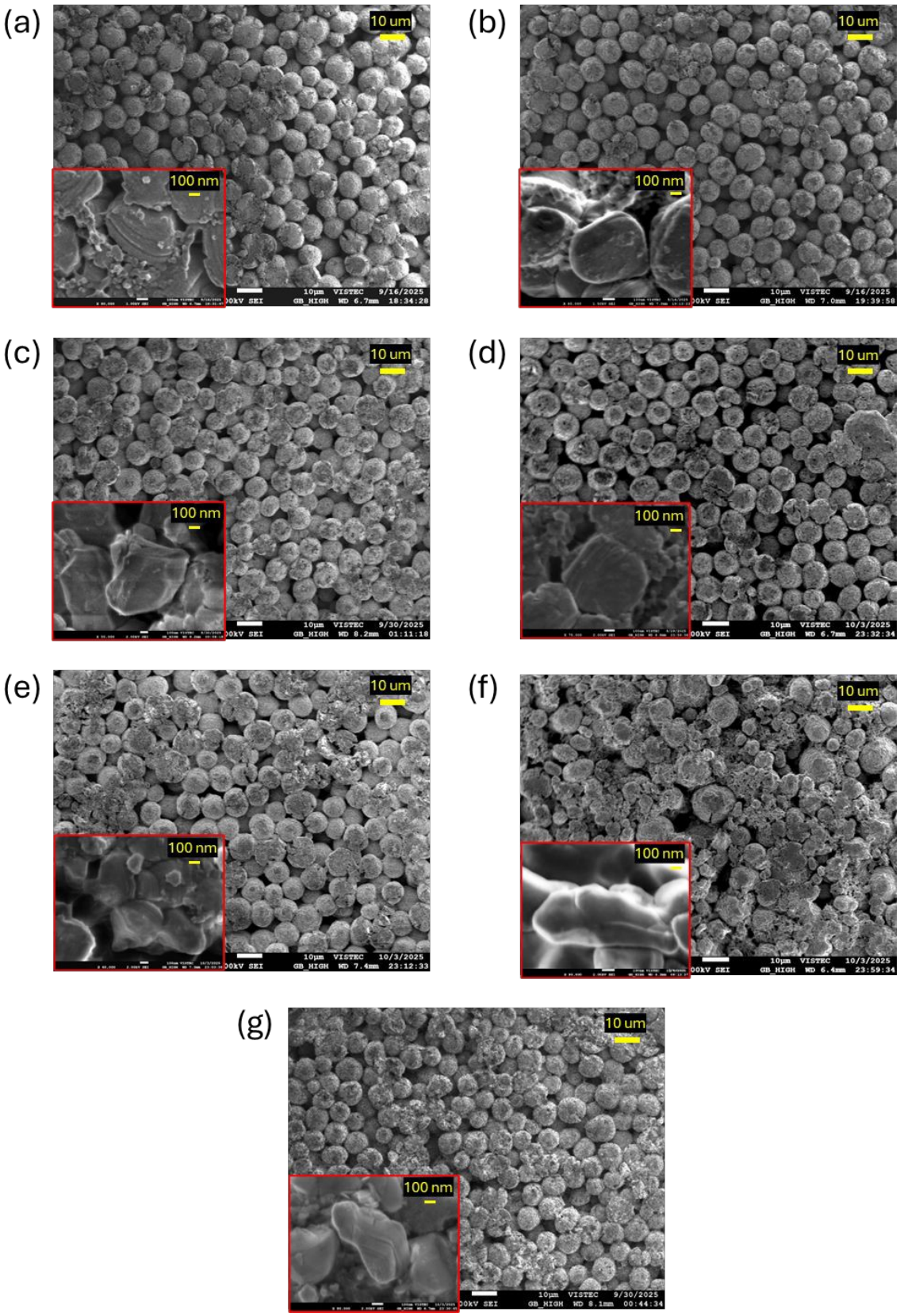

View Article Online
DOI: 10.1039/D6SC03512D

Open Access Article. Published on 22 June 2026. Downloaded on 6/23/2026 5:02:46 AM.
This article is licensed under a Creative Commons Attribution-NonCommercial 3.0 Unported Licence.

Figure 5. Post-cycling surface morphology of NMC90 cathodes in electrolytes with different fluorinated carbonate additives. FESEM images after 500 cycles for electrodes cycled in (a) reference electrolyte, (b) FEC-, (c) DFEC-containing electrolyte, and linear fluorinated carbonate electrolytes containing (d) FDEC-, (e) DFDEC-, (f) TFDEC-, and (g) TTFDEC- containing electrolyte. Low-magnification images (scale bar: 10 μm) illustrate the integrity of secondary particles, while high-magnification insets (scale bar: 100 nm) highlight surface features and primary-particle degradation.

3.6 Nanoscale Interphase Architecture Revealed by TEM, EDS, and SAED

Cross-sectional TEM and EDS were performed on both electrodes after 500 cycles to directly visualize interphase thickness and elemental composition in the DFEC-based system (Figure 6), complemented by SAED for crystallographic phase identification of the anode SEI (Figure S26, Table S6).

Anode SEI (Figure 6a). The DFEC-derived SEI is laterally continuous and conformal, with local thickness measurements of 167.63, 206.65, and 223.09 nm. The defining feature is not absolute thickness but morphological uniformity: the absence of delamination, cracking, void formation, or porous heterogeneities reflects simultaneous, homogeneous SEI nucleation driven by DFEC's preferential reductive decomposition within the Li^+ first coordination shell (CN = 0.183) — in contrast to the patchy growth expected from uncontrolled carbonate reduction. This is fully consistent with the low AFM surface roughness (Sq = 0.153 μm), minimal valley void volume (VVV = 3.98×10^{-9} ml/m²), and well-resolved single-arc anode impedance response in in situ EIS (Figure 7).

Chemical Science Accepted Manuscript

View Article Online
DOI: 10.1039/D6SC03512D

Open Access Article. Published on 22 June 2026. Downloaded on 6/23/2026 5:02:46 AM.
This article is licensed under a Creative Commons Attribution-NonCommercial 3.0 Unported Licence.

SAED Phase Identification (Figure S26, Table S6). Three polycrystalline diffraction rings are indexed unambiguously to LiF (111, d = 2.33 Å; 200, d = 2.07 Å), Li_2O (002, d = 2.31 Å), and Li_2CO_3 (31-1, d = 2.18 Å), all with $\Delta\% < 3.2\%$, confirming that the inorganic SEI framework is stoichiometrically intact and well-crystallized after 500 cycles. LiF — identified through two independent reflections — provides electronic passivation and selective Li^+ conduction at grain boundaries; Li_2O contributes ionic conductivity and acts as a ductile buffer phase; and Li_2CO_3 bridges the inorganic inner SEI with the organic outer layer identified by F 1s XPS (Figure 9e, g). This multi-component inorganic architecture, enabled exclusively by DFEC's solvation-active decomposition pathway, is corroborated by the depth-persistent LiF signal in XPS, compact TEM morphology, and low anode impedance.

Cathode CEI (Figure 6b). The DFEC-derived CEI is substantially thinner (26.70–90.79 nm) than the anode SEI by approximately one order of magnitude, consistent with a self-limiting growth mechanism: directed DFEC oxidative decomposition deposits a passivating LiF-rich CEI during early cycling, after which the electronically insulating interphase kinetically suppresses further electrolyte oxidation. The local thickness variation (~27–91 nm) reflects spatially adaptive deposition — thicker accumulation at reactive grain-boundary step-edges and thinner coverage over flat crystal facets — a hallmark of solvation-directed interphase formation that stands in contrast to the indiscriminate, thick CEI growth produced by solvation-inactive additives. This thin, conformal CEI directly underpins the low cathode charge-transfer resistance and NMC90 morphological preservation confirmed by FESEM (Figure 5c) and AFM (Figure S24).

EDS Analysis (Figure 6c–d). At the anode, dominant C Kα and O Kα signals are consistent with the organic/inorganic SEI composition identified by XPS and SAED. A weak P Kα signal confirms only minor $LiPF_6$ decomposition contribution, confirming that the SEI is dominated by additive

Chemical Science Accepted Manuscript

View Article Online
DOI: 10.1039/D6SC03512D

rather than salt decomposition products. Low-intensity transition-metal signals indicate limited Ni crossover from NMC90, consistent with effective CEI passivation. At the cathode, well-resolved Ni, Co, and Mn Kα lines reflect preserved NMC90 bulk stoichiometry without detectable Ni depletion or rock-salt reconstruction — anomalies that would be expected in poorly passivated systems such as TFDEC-based cells.

Integrated Interpretation. TEM, EDS, and SAED together establish a self-consistent nanoscale portrait: a conformal, crystallographically robust SEI (LiF + Li_2O + Li_2CO_3) at the anode and a thin, topography-adaptive CEI at the cathode, simultaneously achieved through DFEC's active solvation participation. This dual-electrode interphase quality is the defining nanoscale signature

Open Access Article. Published on 22 June 2026. Downloaded on 6/23/2026 5:02:46 AM.
This article is licensed under a Creative Commons Attribution-NonCommercial 3.0 Unported Licence.

Chemical Science Accepted Manuscript

View Article Online
DOI: 10.1039/D6SC03512D

Open Access Article. Published on 22 June 2026. Downloaded on 6/23/2026 5:02:46 AM.
This article is licensed under a Creative Commons Attribution-NonCommercial 3.0 Unported Licence.

that accounts for DFEC's superior capacity retention, morphological stability, and charge-transfer kinetics relative to all solvation-inactive fluorinated additives in this study.

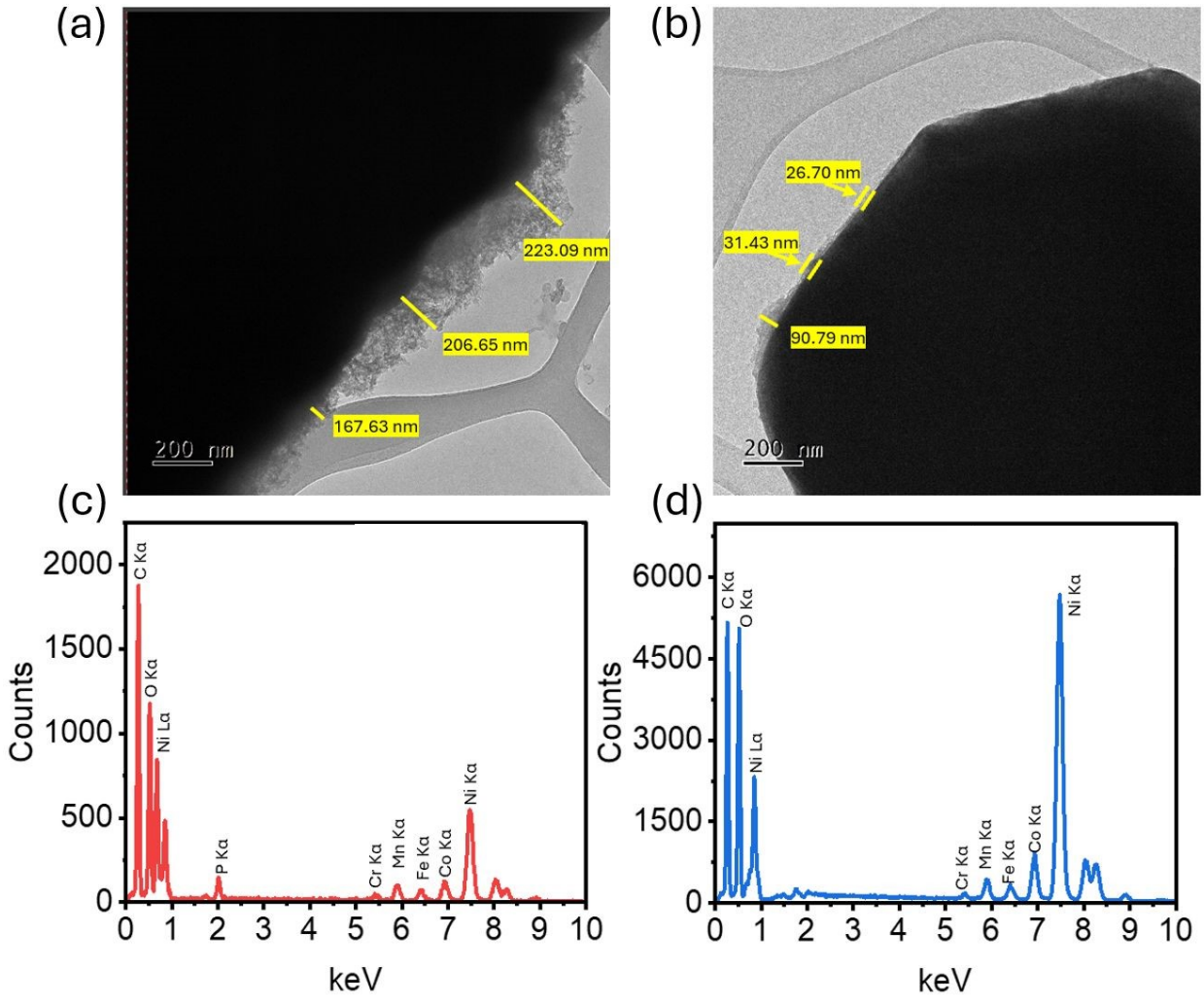

Figure 6. TEM images and EDS spectra of the electrodes after 500 cycles in the DFEC-containing electrolyte: (a) TEM image of the anode showing SEI layer thickness, (b) TEM image of the cathode showing CEI layer thickness, (c) EDS spectrum of the anode surface, and (d) EDS spectrum of the cathode surface.

Chemical Science Accepted Manuscript

View Article Online
DOI: 10.1039/D6SC03512D

Open Access Article. Published on 22 June 2026. Downloaded on 6/23/2026 5:02:46 AM.
This article is licensed under a Creative Commons Attribution-NonCommercial 3.0 Unported Licence.

3.7 Charge-Transfer Kinetics and Interphase Evolution Probed by In Situ EIS

In situ EIS was performed on the NMC90 cathode during charging to 4.3 V and the graphite anode during discharging to 0.01 V vs. Li/Li^+ (Figure 7), with complementary data for every condition provided in Figure S27 and S28.

Cathode Impedance Evolution. The reference electrolyte (Figure 7a) exhibits progressive Rct growth from ~15–20 Ω at low states of charge to ~45–50 Ω near 4.3 V, with increasingly distorted arcs at high potentials reflecting continuous CEI reconstruction from uncontrolled carbonate oxidation. The DFEC-based cathode (Figure 7b) shows a qualitatively distinct trajectory: Rct increases modestly from ~10–15 Ω to ~40–45 Ω across the full charging window, but crucially, the semicircular arcs remain geometrically well-defined and undistorted throughout — indicating a chemically uniform, stable CEI formed via preferential DFEC decomposition within the Li^+ solvation shell that suppresses subsequent oxidative side reactions and maintains facile, kinetically well-defined Li^+ transport. In contrast, the TFDEC-based cathode (Figure 7c) develops a secondary low-frequency semicircular feature and overall spectral distortion at intermediate-to-high potentials, with Rct approaching ~45–50 Ω at 4.3 V — signatures of a heterogeneous, multi-layered CEI arising from uncontrolled carbonate decomposition in the absence of solvation-directed interphase formation, consistent with the severe NMC90 structural degradation observed by FESEM (Figure 5f).

Anode Impedance Evolution. The reference electrolyte anode (Figure 7d) shows a broad, flat response with multiple overlapping relaxation features ($Z'' \leq$ ~200 Ω), indicative of competing uncontrolled reduction pathways producing a heterogeneous SEI. The DFEC-based anode (Figure 7e) exhibits a strikingly different behavior: well-resolved, large-amplitude semicircles peaking at Z'' ~300–400 Ω at intermediate discharge potentials, decreasing systematically toward 0.01 V as

Chemical Science Accepted Manuscript

View Article Online
DOI: 10.1039/D6SC03512D

the DFEC-derived SEI becomes fully conditioned. The single-semicircle character and systematic potential dependence confirm that SEI formation proceeds through a single, well-defined reduction mechanism governed by DFEC solvation participation, directly underpinning the thin, smooth, continuous SEI morphology observed by FESEM and the low valley void volume confirmed by AFM (Figure S24). The TFDEC-based anode (Figure 7f) shows low overall impedance ($Z'' \leq \sim 150$ Ω) but with strongly distorted, erratically evolving Nyquist features and pronounced low-frequency tails — indicative not of facile kinetics but of a porous, non-uniform SEI with distributed local resistances arising from uncontrolled carbonate co-reduction, consistent with the cracked SEI morphology observed by FESEM (Figure S25).

Full Series Trends. FEC produces cathode and anode EIS responses qualitatively similar to DFEC with well-resolved, regularly evolving semicircles. FDEC and DFDEC display intermediate behavior with partially defined arcs, reflecting partial solvation participation and intermediate interphase quality. TTFDEC closely resembles TFDEC, confirming that excessive linear-carbonate fluorination systematically excludes the additive from the Li^+ coordination shell and drives non-selective interphase formation at both electrodes.

Taken together, in situ EIS establishes that the degree of additive participation in the Li^+ solvation shell directly governs charge-transfer kinetics at both electrodes: solvation-active additives (DFEC, FEC) yield geometrically regular, kinetically facile interfaces, while solvation-excluded additives (TFDEC, TTFDEC) produce heterogeneous, ionically resistive interphases that drive accelerated capacity fading in full-cell cycling.

Open Access Article. Published on 22 June 2026. Downloaded on 6/23/2026 5:02:46 AM.
This article is licensed under a Creative Commons Attribution-NonCommercial 3.0 Unported Licence.

Chemical Science Accepted Manuscript

View Article Online
DOI: 10.1039/D6SC03512D

Open Access Article. Published on 22 June 2026. Downloaded on 6/23/2026 5:02:46 AM.
This article is licensed under a Creative Commons Attribution-NonCommercial 3.0 Unported Licence.

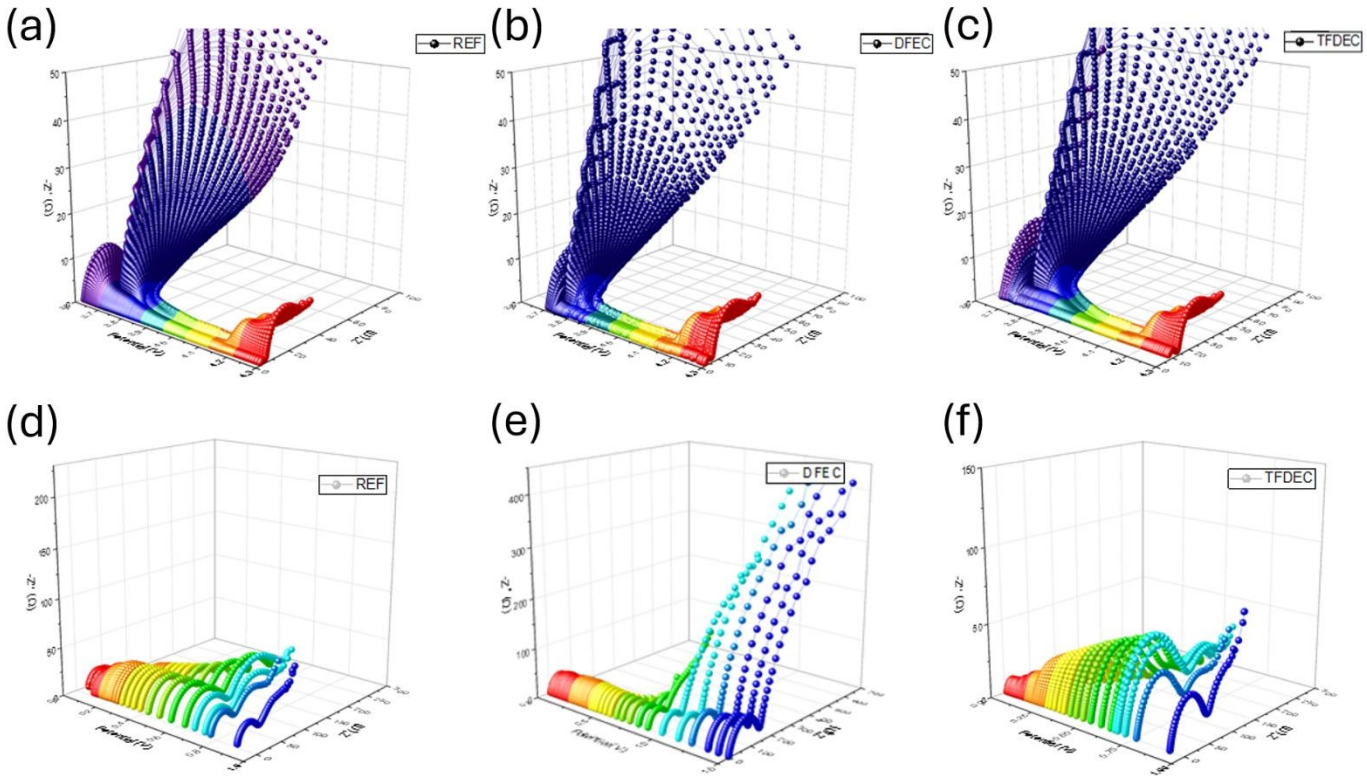

Figure 7. 3D evolution of *in situ* electrochemical impedance spectroscopy (EIS) spectra. (a–c) represent the impedance evolution of the **cathode** during charging from 3.6 to 4.3 V vs. Li/Li^+, and (d–f) represent the anode from 0.0 to 1.0 V vs. Li/Li^+, comparing the baseline electrolyte (REF) with fluorinated additives (DFEC and TFDEC).

3.8 Temperature-Dependent Interfacial Kinetics and Activation Energy Penalties

Temperature-dependent electrochemical impedance spectroscopy (EIS) was employed to elucidate the influence of fluorinated solvation structures and SEI chemistry on interfacial charge-transfer kinetics in selected graphite anodes (Figure 8). Measurements were conducted over the temperature range from -10 to 30 C, and representative Nyquist plots together with equivalent-circuit fittings are presented in Figure S29. The detailed analysis of series resistance, contact resistance, and charge transfer resistance for the cathode half-cells using various electrolytes is provided in Table S6-S12. Similarly, the corresponding resistance parameters for the anode half-

Chemical Science Accepted Manuscript

View Article Online
DOI: 10.1039/D6SC03512D

Open Access Article. Published on 22 June 2026. Downloaded on 6/23/2026 5:02:46 AM.
This article is licensed under a Creative Commons Attribution-NonCommercial 3.0 Unported Licence.

cells are detailed in Table S13-S19. Additional anode EIS data and the corresponding cathode responses are provided in Figure S30 and S31, respectively. At 30 °C, graphite anodes with DFEC- and TFDEC-containing electrolytes exhibit similarly low charge-transfer resistances, with R_{ct} values of approximately 12 Ω and 11 Ω, respectively, indicating facile Li^+ transfer across the electrode–electrolyte interface under near-ambient conditions. Upon cooling, however, a pronounced divergence emerges. At −10 °C, the DFEC-based electrolyte shows only a moderate increase in R_{ct} to ~60 Ω, whereas the TFDEC-based electrolyte displays a dramatic rise to ~470 Ω, signifying severely hindered interfacial charge transfer at low temperature [38]. This strong contrast demonstrates that, despite comparable interfacial kinetics at 30 °C, the TFDEC-derived interphase becomes substantially more resistive upon cooling, which directly accounts for the inferior low-temperature performance and accelerated capacity fading observed for TFDEC-containing cells. The temperature dependence of the anode charge-transfer resistance for all electrolyte formulations is further analyzed using Arrhenius plots (Figure 8c). All systems exhibit approximately linear behavior, confirming that charge transfer at the graphite SEI is a thermally activated process. At any given temperature, R_{ct} is the highest for TFDEC-containing electrolytes, while FEC- and DFEC-based electrolytes consistently show the lowest values. Notably, the slopes of the Arrhenius lines differ significantly among formulations, reflecting distinct activation barriers for interfacial charge transfer. Electrolytes containing DFDEC, TFDEC, and TTFDEC exhibit the steepest slopes, indicating a strong sensitivity of R_{ct} to temperature, whereas FEC, FDEC, and DFEC based electrolytes display shallower slopes, corresponding to more temperature-tolerant interfacial kinetics. Figure 8d quantifies these trends by extracting activation energies (E_a) from the Arrhenius fits. The reference electrolyte exhibits an E_a of 0.56 eV, which is modestly reduced in the presence of FEC-based electrolyte (0.51 eV) and more substantially lowered by

Chemical Science Accepted Manuscript

View Article Online
DOI: 10.1039/D6SC03512D

DFEC-based electrolyte (0.40 eV), demonstrating that cyclic fluorinated carbonates effectively facilitate Li^+ desolvation and charge transfer across the graphite SEI. In contrast, linear fluorinated additives impose higher energetic barriers: FDEC- and DFDEC-based electrolytes yield E_a values of 0.55 and 0.59 eV, respectively, while the highly fluorinated TFDEC- and TTFDEC- based electrolytes show the largest activation energies (0.71 and 0.63 eV). These elevated barriers explain the pronounced increase in R_{ct} at sub-ambient temperatures and the associated kinetic limitations.

Collectively, these results establish that cyclic fluorinated additives—particularly DFEC—most effectively reduce the energetic barrier for interfacial charge transfer, whereas excessive fluorination in linear carbonates leads to kinetically unfavorable, temperature-sensitive interphases that impose severe penalties on low-temperature performance. These pronounced differences in charge-transfer resistance and activation energy have severe implications for practical battery deployment in sub-ambient climates. The lower interfacial activation energy enabled by active-solvation components (e.g., DFEC: 0.40 eV) directly translates into excellent cold-climate resilience, maintaining a functional R_{ct} of only ~60 Ω even at -10 °C (Figure 8a). Conversely, the significantly elevated barrier induced by highly fluorinated linear additives under the solvation exclusion regime (e.g., TFDEC: 0.71 eV) leads to severe kinetic polarization upon cooling, causing a dramatic rise in R_{ct} to ~470 Ω at -10 °C (Figure 8b). These findings explicitly connect molecular-level desolvation penalties to macroscopic transport limitations under realistic sub-ambient operating conditions.

Open Access Article. Published on 22 June 2026. Downloaded on 6/23/2026 5:02:46 AM.
This article is licensed under a Creative Commons Attribution-NonCommercial 3.0 Unported Licence.

Chemical Science Accepted Manuscript

View Article Online
DOI: 10.1039/D6SC03512D

Open Access Article. Published on 22 June 2026. Downloaded on 6/23/2026 5:02:46 AM.
This article is licensed under a Creative Commons Attribution-NonCommercial 3.0 Unported Licence.

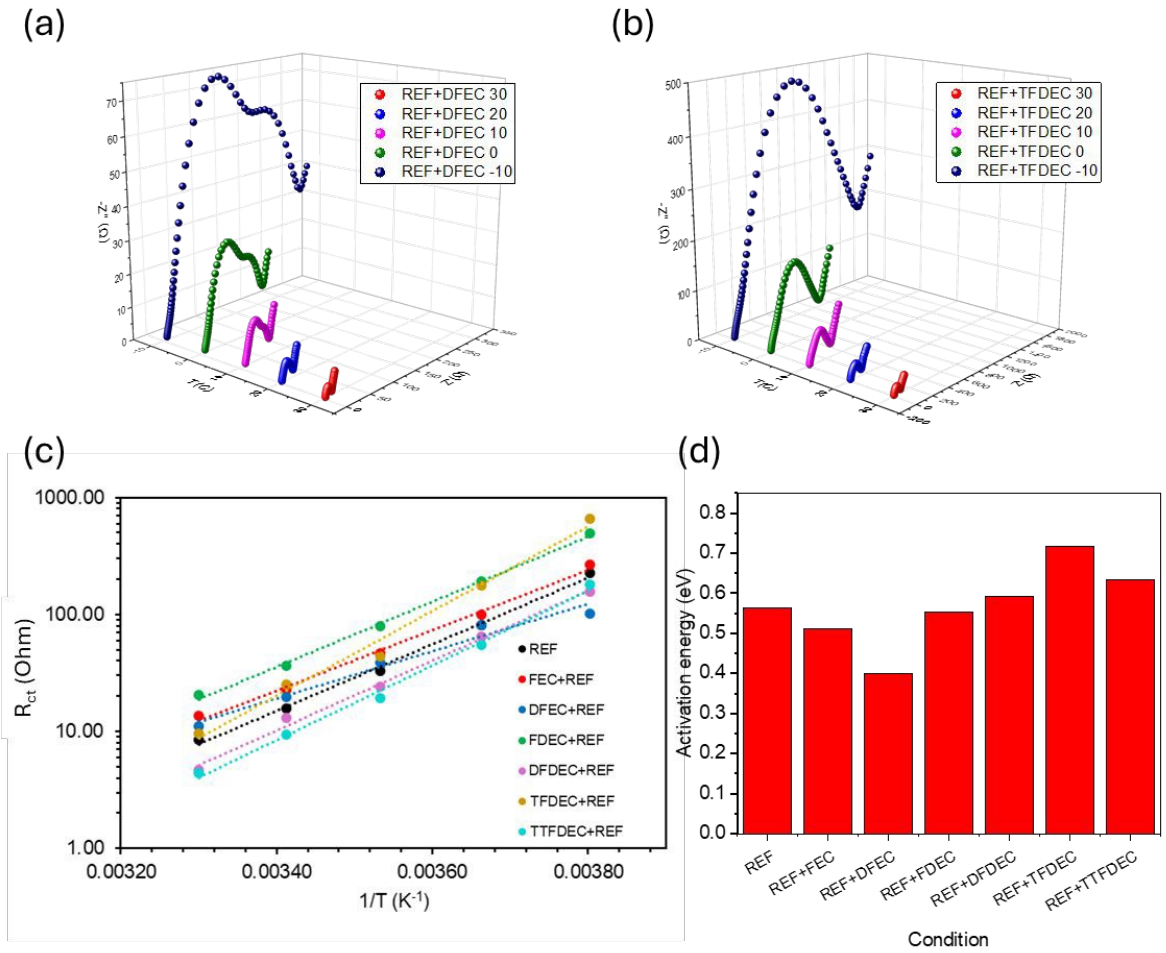

Figure 8. Temperature-dependent interfacial kinetics and charge-transfer activation energies for graphite anodes with fluorinated electrolyte additives. (a) Nyquist plots of graphite half-cells with the reference electrolyte containing DFEC (DFEC + REF ; REF = 1 M $LiPF_6$ in EC:DEC:DMC) measured at different temperatures. (b) Nyquist plots of graphite half-cells with the reference electrolyte containing TFDEC (TFDEC + REF) measured at different temperatures. (c) Arrhenius plots of charge-transfer resistance (R_{ct}) as a function of inverse temperature (1/T) for all electrolyte formulations. (d) Charge-transfer activation energies extracted from Arrhenius fitting of the temperature-dependent R_{ct} data.

3.9 Interphase Chemistry Origin of Kinetic Divergence Revealed by XPS Depth Profiling

Chemical Science Accepted Manuscript

View Article Online
DOI: 10.1039/D6SC03512D

Open Access Article. Published on 22 June 2026. Downloaded on 6/23/2026 5:02:46 AM.
This article is licensed under a Creative Commons Attribution-NonCommercial 3.0 Unported Licence.

XPS depth profiling was conducted on the graphite anodes (Figure 9) and NMC90 cathodes (Figure S32) after 500 cycles to elucidate the chemical compositions of the SEI and CEI. The full datasets for all formulations are summarized in Figure S33 and S34 and Table S20 in Supplementary Information. Both electrochemical performance testing and post-mortem XPS characterization were conducted at a controlled temperature of 25 °C.

Cathode CEI Chemistry (Figure S32). Surface C 1s spectra reveal that the DFEC-based CEI is dominated by C–C (284.8 eV) with only modest C–O, C=O, and O–C=O contributions, indicating a thin, inorganically rich interphase with limited organic decomposition product accumulation. The TFDEC-based cathode shows markedly enhanced C=O and O–C=O intensities relative to C–C, consistent with continuous uncontrolled carbonate oxidation at the NMC90 surface. After 20 s Ar^+ sputtering, the DFEC cathode retains predominantly C–C character with rapid organic signal attenuation, confirming a thin, well-defined CEI, while TFDEC shows persistent C–O and O–C=O features at depth, indicating a thicker, organically heterogeneous interphase.

The F 1s depth profiles provide the most compelling differentiation. The DFEC cathode surface (Figure S32e) is overwhelmingly dominated by LiF (685.3 eV) with only minor P–F (~687.3 eV) and C–F (~688.8 eV) contributions, directly reflecting directed DFEC decomposition within the Li^+ solvation shell. The TFDEC cathode (Figure S32f) shows relatively larger C–F and P–F components alongside LiF, characteristic of non-selective fluorinated carbonate and $LiPF_6$ decomposition. After sputtering (Figure S32g–h), the DFEC cathode retains a highly intense, narrow LiF peak with negligible P–F and C–F contributions at depth — confirming spatially uniform LiF enrichment throughout the inner CEI — while the TFDEC cathode shows a diminished LiF signal with elevated organic-F and phosphate features, establishing an organically rich, LiF-deficient inner interphase.

Chemical Science Accepted Manuscript

View Article Online
DOI: 10.1039/D6SC03512D

Open Access Article. Published on 22 June 2026. Downloaded on 6/23/2026 5:02:46 AM.
This article is licensed under a Creative Commons Attribution-NonCommercial 3.0 Unported Licence.

Anode SEI Chemistry (Figure 9). Surface C 1s spectra of both DFEC- and TFDEC-based anodes are dominated by C–C (284.8 eV) with comparable minor C–O, C=O, and O–C=O contributions, indicating similarly thin organic outer SEI layers on graphite. After 20 s sputtering, higher-binding-energy components attenuate in both cases, confirming thin SEIs with graphite-dominated sub-surfaces. The critical differentiation again emerges in F 1s: at the surface, both systems show a dominant LiF peak at 685.3 eV alongside weaker P–F and C–F features. After sputtering (Figure 9g–h), the DFEC anode retains a highly intense LiF signal with only minor P–F and C–F contributions at depth, demonstrating LiF enrichment throughout the inner SEI, while the TFDEC anode shows reduced LiF intensity with relatively stronger C–F and P–F features — confirming a more organic- and phosphate-rich inner SEI with significantly lower LiF content.

Integrated Interpretation. C 1s and F 1s depth profiles at both electrodes reveal a fully self-consistent, electrode-symmetric picture: DFEC participation in the Li^+ solvation shell directs the formation of LiF-rich, inorganically dominated interphases extending throughout the sub-surface at both cathode and anode, while TFDEC exclusion from the solvation shell yields comparatively organic- and phosphate-rich interphases with lower LiF content at depth on both electrode surfaces. This fundamental difference in interphase chemistry provides the direct mechanistic explanation for DFEC's superior interfacial stability, lower charge-transfer resistance, and improved long-term cycling kinetics, confirming that solvation-shell participation by moderately

Chemical Science Accepted Manuscript

View Article Online
DOI: 10.1039/D6SC03512D

fluorinated cyclic additives is the decisive molecular-level determinant of interphase quality in high-energy Ni-rich full cells.

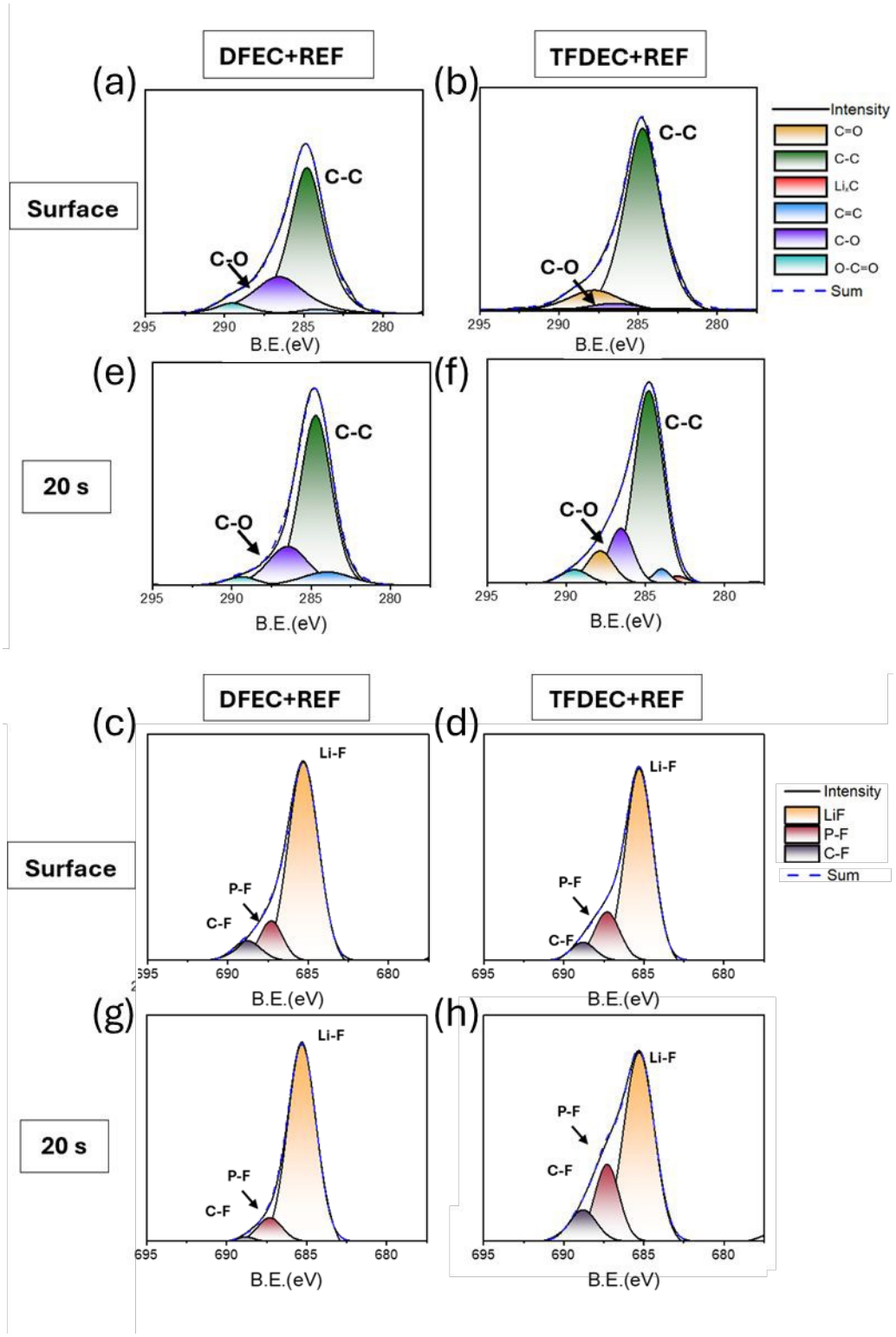

Open Access Article. Published on 22 June 2026. Downloaded on 6/23/2026 5:02:46 AM.
This article is licensed under a Creative Commons Attribution-NonCommercial 3.0 Unported Licence.

Chemical Science Accepted Manuscript

View Article Online
DOI: 10.1039/D6SC03512D

Open Access Article. Published on 22 June 2026. Downloaded on 6/23/2026 5:02:46 AM.
This article is licensed under a Creative Commons Attribution-NonCommercial 3.0 Unported Licence.

Figure 9. XPS depth-profile analysis of graphite anodes cycled in electrolytes containing DFEC and TFDEC additives. (a, b) C 1s spectra of anode surfaces after cycling in DFEC- and TFDEC-containing reference electrolytes (REF = 1 M $LiPF_6$ in EC:DEC:DMC), respectively. (c, d) Corresponding F 1s spectra of the anode surfaces. (e, f) C 1s spectra after 20 s Ar^+ sputtering for DFEC- and TFDEC-based electrolytes, respectively. (g, h) F 1s spectra after 20 s Ar^+ sputtering, highlighting the distribution of LiF, P–F, and C–F species within the SEI.

3.10 Integrated Performance Map and Electrolyte Design Principles

Figure 10 presents a radar chart that consolidates the key electrochemical performance metrics of all electrolyte formulations, with each parameter normalized to facilitate direct comparison. The evaluated metrics include rate capability, long-term capacity retention, Li^+ transference number, contact ion-pair (CIP) population, Li^+ diffusion coefficients extracted from GITT measurements, and the charge-transfer activation energy derived from Arrhenius analysis. Electrolytes containing cyclic fluorinated additives, particularly FEC and DFEC, exhibit the largest enclosed areas, indicating a well-balanced combination of fast Li^+ transport, high-rate capability, stable cycling retention, moderate CIP formation, and reduced interfacial activation barriers. In contrast, electrolytes incorporating highly fluorinated linear additives (TFDEC and TTFDEC) display markedly contracted profiles, characterized by poor rate performance, suppressed Li^+ diffusion, and elevated activation energies, consistent with sluggish interfacial kinetics and inferior low-temperature behavior. The reference electrolyte, together with FDEC- and DFDEC-based systems, occupies an intermediate regime, reflecting trade-offs between transport efficiency, interfacial kinetics, and long-term stability. Overall, this comparative visualization highlights that an

Chemical Science Accepted Manuscript

View Article Online
DOI: 10.1039/D6SC03512D

optimized degree of fluorination—most effectively achieved with cyclic carbonate additives—yields the most favorable balance between solvation chemistry and electrochemical performance. This comprehensive evaluation highlights the direct manifestation of solvation-directed interphase chemistry on practically relevant cell metrics across multiple demanding conditions (such as low-temperature operation, high-rate fast charging, and high-voltage energy-dense configurations). To systematically visualize these multi-dimensional effects, the integrated performance profiles are mapped onto a holistic radar chart (Figure 10). Electrolytes maintaining active solvation (such as FEC and DFEC) display a highly balanced, well-rounded profile that satisfies all practical constraints simultaneously. In contrast, highly fluorinated linear systems (such as TFDEC and TTFDEC) exhibit heavily contracted profiles driven by their intrinsic kinetic failure and lack of cell-wide passivation, underscoring that practical commercial viability requires a careful structural balance between fluorination degree and molecular geometry.

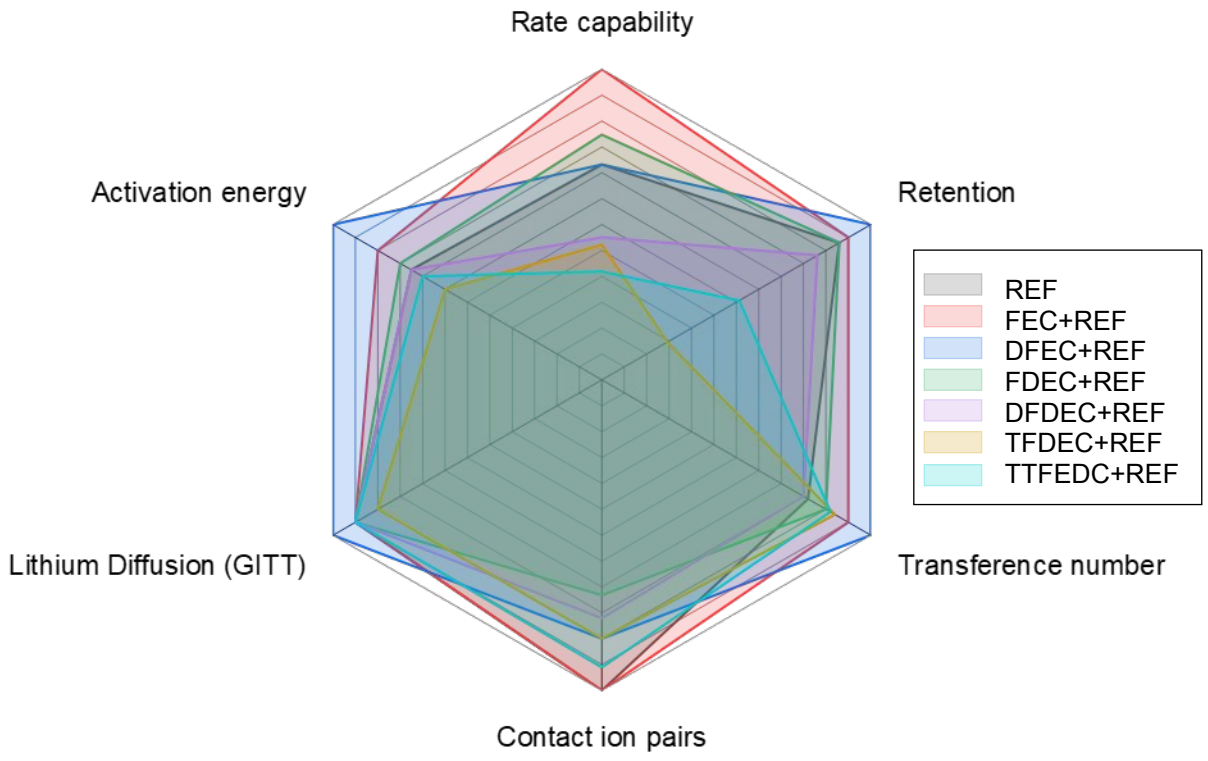

Open Access Article. Published on 22 June 2026. Downloaded on 6/23/2026 5:02:46 AM.
This article is licensed under a Creative Commons Attribution-NonCommercial 3.0 Unported Licence.

Chemical Science Accepted Manuscript

View Article Online
DOI: 10.1039/D6SC03512D

Open Access Article. Published on 22 June 2026. Downloaded on 6/23/2026 5:02:46 AM.
This article is licensed under a Creative Commons Attribution-NonCommercial 3.0 Unported Licence.

Figure 10. Radar chart summarizing and comparing key electrochemical performance metrics for all electrolyte formulations, including the reference electrolyte (1 M $LiPF_6$ in EC: DEC: DMC) and electrolytes containing cyclic and linear fluorinated carbonate additives. The plotted parameters integrate solvation–transport–interfacial effects, encompassing initial coulombic efficiency, rate capability, long-term capacity retention, Li^+ transference number, charge-transfer activation energy, and interfacial stability indicators derived from electrochemical and spectroscopic analyses. Larger enclosed areas indicate a more balanced and overall superior electrolyte performance.

4. Conclusion

In this work, we systematically elucidate how fluorination degree and molecular geometry (cyclic versus linear) in fluorinated carbonate electrolytes dictate Li^+ solvation chemistry, interfacial kinetics, and long-term electrochemical stability in Ni-rich NMC90 cells. By integrating DFT and MD simulations, DOSY NMR spectroscopy, electrochemical diagnostics (rate capability, long-term cycling, GITT, and temperature-dependent Arrhenius analysis), and post-mortem structural and chemical characterization (SEM, XPS, TEM and AFM), we establish a unified, multiscale understanding of fluorination-controlled electrolyte behavior.

Our results reveal that moderate fluorination combined with cyclic molecular geometry optimally tunes Li^+–solvent interactions, yielding well-organized solvation shells, favorable contact-ion-pair populations, and reduced desolvation barriers. In particular, the DFEC-based electrolyte achieves the lowest charge-transfer activation energy, promotes efficient Li^+ transport, and enables the formation of a LiF-rich, inorganic-dominated SEI that penetrates deeply into the interphase. This

Chemical Science Accepted Manuscript

View Article Online
DOI: 10.1039/D6SC03512D

Open Access Article. Published on 22 June 2026. Downloaded on 6/23/2026 5:02:46 AM.
This article is licensed under a Creative Commons Attribution-NonCommercial 3.0 Unported Licence.

synergistic solvation–interphase coupling translates into superior electrochemical performance, including high rate capability (90.81 mAh g^{-1} at high C-rate) and stable long-term cycling (92.59 mAh g^{-1} after 500 cycles).

In contrast, strongly fluorinated linear additives (TFDEC and TTFDEC) exhibit excessively weakened Li^+ coordination, leading to exclusion from the primary solvation shell, elevated charge-transfer activation energies, resistive interphases, and severe performance degradation, with only 36–42% capacity retention after extended cycling. SEM and XPS analyses corroborate these findings, revealing extensive particle cracking and organic-rich, LiF-deficient SEI structures in highly fluorinated linear systems.

Collectively, this study establishes clear mechanistic design rules for fluorinated electrolytes: effective additives must balance electron-withdrawing fluorination with sufficient Lewis basicity to remain active in Li^+ solvation, while simultaneously enabling low-barrier charge transfer and chemically robust interphases. These criteria are most effectively satisfied by cyclic fluorinated carbonates at moderate fluorination levels, whereas linear fluorinated additives require careful compositional tuning to avoid kinetic and interfacial penalties. The insights presented here provide a rational framework for the next generation of high-performance electrolytes tailored for Ni-rich cathodes and advanced lithium-ion batteries.

Chemical Science Accepted Manuscript

Acknowledgement

This work was financially supported under Program Management Unit for National Competitiveness Enhancement (PMUC) by Office of National Higher Education Science Research and Innovation Policy Council (NXPO) and IRPC Public Company Limited, Thailand Science Research and Innovation (TSRI) under the Fundamental Fund, and Energy Conservation and

View Article Online
DOI: 10.1039/D6SC03512D

Promotion Fund (ENCON FUND), Ministry of Energy, Thailand. In addition, the Frontier Research Centre (FRC) at Vidyasirimedhi Institute of Science and Technology (VISTEC) supported this work. T. S. gratefully acknowledges VISTEC for financial support through the M.Eng. scholarship program. Characterization facilities and technical support were provided by the Frontier Research Centre at VISTEC.

Open Access Article. Published on 22 June 2026. Downloaded on 6/23/2026 5:02:46 AM.
This article is licensed under a Creative Commons Attribution-NonCommercial 3.0 Unported Licence.

Chemical Science Accepted Manuscript

References

[1] J.W. Choi, D. Aurbach, Promise and reality of post-lithium-ion batteries with high energy densities, Nature Reviews Materials 1(4) (2016) 16013. https://doi.org/10.1038/natrevmats.2016.13.
[2] F. Duffner, N. Kronemeyer, J. Tübke, J. Leker, M. Winter, R. Schmuch, Post-lithium-ion battery cell production and its compatibility with lithium-ion cell production infrastructure, Nature Energy 6(2) (2021) 123-134. https://doi.org/10.1038/s41560-020-00748-8.
[3] M. Li, J. Lu, Z. Chen, K. Amine, 30 Years of Lithium-Ion Batteries, Advanced Materials 30(33) (2018) 1800561. https://doi.org/https://doi.org/10.1002/adma.201800561.
[4] Foreword by Jeff Dahn, in: K. Xu (Ed.), Electrolytes, Interfaces and Interphases, The Royal Society of Chemistry2023, p. 0. https://doi.org/10.1039/9781839166174-FP009.
[5] K. Xu, Electrolytes and Interphases in Li-Ion Batteries and Beyond, Chemical Reviews 114(23) (2014) 11503-11618. https://doi.org/10.1021/cr500003w.
[6] F. Lin, I.M. Markus, D. Nordlund, T.-C. Weng, M.D. Asta, H.L. Xin, M.M. Doeff, Surface reconstruction and chemical evolution of stoichiometric layered cathode materials for lithium-ion batteries, Nature Communications 5(1) (2014) 3529. https://doi.org/10.1038/ncomms4529.
[7] R. Jung, M. Metzger, F. Maglia, C. Stinner, H.A. Gasteiger, Oxygen Release and Its Effect on the Cycling Stability of LiNixMnyCozO2 (NMC) Cathode Materials for Li-Ion Batteries, Journal of The Electrochemical Society 164(7) (2017) A1361. https://doi.org/10.1149/2.0021707jes.
[8] J. Wandt, A.T.S. Freiberg, A. Ogrodnik, H.A. Gasteiger, Singlet oxygen evolution from layered transition metal oxide cathode materials and its implications for lithium-ion batteries, Materials Today 21(8) (2018) 825-833. https://doi.org/https://doi.org/10.1016/j.mattod.2018.03.037.
[9] J. Cabana, L. Monconduit, D. Larcher, M.R. Palacín, Beyond Intercalation-Based Li-Ion Batteries: The State of the Art and Challenges of Electrode Materials Reacting Through Conversion Reactions, Advanced Materials 22(35) (2010) E170-E192. https://doi.org/https://doi.org/10.1002/adma.201000717.

View Article Online
DOI: 10.1039/D6SC03512D

[10] D.J. Yoo, Q. Liu, O. Cohen, M. Kim, K.A. Persson, Z. Zhang, Understanding the Role of SEI Layer in Low-Temperature Performance of Lithium-Ion Batteries, ACS Appl Mater Interfaces 14(9) (2022) 11910-11918. https://doi.org/10.1021/acsami.1c23934.
[11] A. Abouimrane, I. Belharouak, K. Amine, Sulfone-based electrolytes for high-voltage Li-ion batteries, Electrochemistry Communications 11(5) (2009) 1073-1076. https://doi.org/https://doi.org/10.1016/j.elecom.2009.03.020.
[12] R. Jung, M. Metzger, D. Haering, S. Solchenbach, C. Marino, N. Tsiouvaras, C. Stinner, H.A. Gasteiger, Consumption of Fluoroethylene Carbonate (FEC) on Si-C Composite Electrodes for Li-Ion Batteries, Journal of The Electrochemical Society 163(8) (2016) A1705. https://doi.org/10.1149/2.0951608jes.
[13] O. Lavi, S. Luski, N. Shpigel, C. Menachem, Z. Pomerantz, Y. Elias, D. Aurbach, Electrolyte Solutions for Rechargeable Li-Ion Batteries Based on Fluorinated Solvents, ACS Applied Energy Materials 3(8) (2020) 7485-7499. https://doi.org/10.1021/acsaem.0c00898.
[14] L. Liu, S. Wang, Z. Zhang, J. Fan, W. Qi, S. Chen, Fluoroethylene carbonate as an electrolyte additive for improving interfacial stability of high-voltage LiNi0.6Co0.2Mn0.2O2 cathode, Ionics 25(3) (2019) 1035-1043. https://doi.org/10.1007/s11581-018-2641-0.
[15] E.R. Logan, D.S. Hall, M.M.E. Cormier, T. Taskovic, M. Bauer, I. Hamam, H. Hebecker, L. Molino, J.R. Dahn, Ester-Based Electrolytes for Fast Charging of Energy Dense Lithium-Ion Batteries, The Journal of Physical Chemistry C 124(23) (2020) 12269-12280. https://doi.org/10.1021/acs.jpcc.0c02370.
[16] A.L. Michan, B.S. Parimalam, M. Leskes, R.N. Kerber, T. Yoon, C.P. Grey, B.L. Lucht, Fluoroethylene Carbonate and Vinylene Carbonate Reduction: Understanding Lithium-Ion Battery Electrolyte Additives and Solid Electrolyte Interphase Formation, Chemistry of Materials 28(22) (2016) 8149-8159. https://doi.org/10.1021/acs.chemmater.6b02282.
[17] J. Cabana, L. Monconduit, D. Larcher, M.R. Palacín, Beyond intercalation-based Li-ion batteries: the state of the art and challenges of electrode materials reacting through conversion reactions, Adv Mater 22(35) (2010) E170-92. https://doi.org/10.1002/adma.201000717.
[18] S. Duangdangchote, N. Phattharasupakun, P. Chomkhuntod, P. Chiochan, S. Sarawutanukul, C. Tomon, N. Joraleechanchai, M. Sawangphruk, Effect of fluoroethylene carbonate on the transport property of electrolytes towards Ni-rich Li-ion batteries with high safety, Chemical Communications 57(55) (2021) 6732-6735. https://doi.org/10.1039/D1CC02120F.
[19] D.-J. Yoo, Q. Liu, O. Cohen, M. Kim, K.A. Persson, Z. Zhang, Rational Design of Fluorinated Electrolytes for Low Temperature Lithium-Ion Batteries, Advanced Energy Materials 13(20) (2023) 2204182. https://doi.org/https://doi.org/10.1002/aenm.202204182.
[20] M. Longhini, F. Gebert, F. Conti, A.J. Naylor, Enabling a non-flammable methyl(2,2,2-trifluoroethyl) carbonate electrolyte in NMC622–graphite Li-ion cells by electrode pre-passivation, Energy Advances 3(5) (2024) 1087-1091. https://doi.org/10.1039/D4YA00052H.
[21] W. Ruo, W. Haonan, Z. Huajun, Y. Mingman, L. Zhongbo, Z. Guangzhao, Z. Tong, Q. Yunxian, W. Jun, L. Iseult, D. Yonghong, Highly fluorinated co-solvent enabling ether

Open Access Article. Published on 22 June 2026. Downloaded on 6/23/2026 5:02:46 AM.
This article is licensed under a Creative Commons Attribution-NonCommercial 3.0 Unported Licence.

Chemical Science Accepted Manuscript

View Article Online
DOI: 10.1039/D6SC03512D

electrolyte for high-voltage lithium ion batteries with graphite anode, Energy Materials 3(5) (2023) 300040. https://doi.org/10.20517/energymater.2023.28.
[22] S. Zhou, J. Yang, C. Zhen, M.D. Gu, M. Shao, Utilizing the Elimination Reaction of Linear Fluorinated Carbonate to Stabilize LiCoO2 Cathode up to 4.6 V, Advanced Materials n/a(n/a) (2024) 2410199. https://doi.org/https://doi.org/10.1002/adma.202410199.
[23] J. Guo, F. Hai, W. Chen, X. Gao, Y. Yi, W. Xue, W. Tang, M. Li, Weak Solvation Chemistry in Fluorinated Nonflammable Electrolytes Achieves Stable Cycling in High-Voltage Lithium Metal Batteries, ACS Applied Materials & Interfaces 16(24) (2024) 31056-31066. https://doi.org/10.1021/acsami.4c02848.
[24] Y. Mo, G. Liu, Y. Yin, M. Tao, J. Chen, Y. Peng, Y. Wang, Y. Yang, C. Wang, X. Dong, Y. Xia, Fluorinated Solvent Molecule Tuning Enables Fast-Charging and Low-Temperature Lithium-Ion Batteries, Advanced Energy Materials 13(32) (2023) 2301285. https://doi.org/https://doi.org/10.1002/aenm.202301285.
[25] Z. Yu, W. Yu, Y. Chen, L. Mondonico, X. Xiao, Y. Zheng, F. Liu, S.T. Hung, Y. Cui, Z. Bao, Tuning Fluorination of Linear Carbonate for Lithium-Ion Batteries, Journal of The Electrochemical Society 169(4) (2022) 040555. https://doi.org/10.1149/1945-7111/ac67f5.
[26] X. Cao, P. Gao, X. Ren, L. Zou, M.H. Engelhard, B.E. Matthews, J. Hu, C. Niu, D. Liu, B.W. Arey, C. Wang, J. Xiao, J. Liu, W. Xu, J.-G. Zhang, Effects of fluorinated solvents on electrolyte solvation structures and electrode/electrolyte interphases for lithium metal batteries, Proceedings of the National Academy of Sciences 118(9) (2021) e2020357118. https://doi.org/doi:10.1073/pnas.2020357118.
[27] S. Han, Structure and dynamics in the lithium solvation shell of nonaqueous electrolytes, Scientific Reports 9(1) (2019) 5555. https://doi.org/10.1038/s41598-019-42050-y.
[28] M.T. Ong, O. Verners, E.W. Draeger, A.C.T. van Duin, V. Lordi, J.E. Pask, Lithium Ion Solvation and Diffusion in Bulk Organic Electrolytes from First-Principles and Classical Reactive Molecular Dynamics, The Journal of Physical Chemistry B 119(4) (2015) 1535-1545. https://doi.org/10.1021/jp508184f.
[29] J.L. Schaefer, D.A. Yanga, L.A. Archer, High Lithium Transference Number Electrolytes via Creation of 3-Dimensional, Charged, Nanoporous Networks from Dense Functionalized Nanoparticle Composites, Chemistry of Materials 25(6) (2013) 834-839. https://doi.org/10.1021/cm303091j.
[30] J. Moon, D.O. Kim, L. Bekaert, M. Song, J. Chung, D. Lee, A. Hubin, J. Lim, Non-fluorinated non-solvating cosolvent enabling superior performance of lithium metal negative electrode battery, Nature Communications 13(1) (2022) 4538. https://doi.org/10.1038/s41467-022-32192-5.
[31] Y. Zhao, T. Zhou, M. Mensi, J.W. Choi, A. Coskun, Electrolyte engineering via ether solvent fluorination for developing stable non-aqueous lithium metal batteries, Nature Communications 14(1) (2023) 299. https://doi.org/10.1038/s41467-023-35934-1.
[32] X. Zhang, G. Liu, K. Zhou, T. Jiao, Y. Zou, Q. Wu, X. Chen, Y. Yang, J. Zheng, Enhancing cycle life of nickel-rich LiNi_{0.9}Co_{0.05}Mn_{0.05}O₂ via a highly fluorinated electrolyte additive - pentafluoropyridine, Energy Materials 1(1) (2021) 100005.

Open Access Article. Published on 22 June 2026. Downloaded on 6/23/2026 5:02:46 AM.
This article is licensed under a Creative Commons Attribution-NonCommercial 3.0 Unported Licence.

Chemical Science Accepted Manuscript

View Article Online
DOI: 10.1039/D6SC03512D

[33] J.Z. Olson, C.M. López, E.J.F. Dickinson, Differential Analysis of Galvanostatic Cycle Data from Li-Ion Batteries: Interpretative Insights and Graphical Heuristics, Chemistry of Materials 35(4) (2023) 1487-1513. https://doi.org/10.1021/acs.chemmater.2c01976.
[34] E. Trevisanello, R. Ruess, G. Conforto, F.H. Richter, J. Janek, Polycrystalline and Single Crystalline NCM Cathode Materials—Quantifying Particle Cracking, Active Surface Area, and Lithium Diffusion, Advanced Energy Materials 11(18) (2021) 2003400. https://doi.org/https://doi.org/10.1002/aenm.202003400.
[35] J. Pokharel, A. Cresce, B. Pant, M.Y. Yang, A. Gurung, W. He, A. Baniya, B.S. Lamsal, Z. Yang, S. Gent, X. Xian, Y. Cao, W.A. Goddard, K. Xu, Y. Zhou, Manipulating the diffusion energy barrier at the lithium metal electrolyte interface for dendrite-free long-life batteries, Nature Communications 15(1) (2024) 3085. https://doi.org/10.1038/s41467-024-47521-z.
[36] H. Dai, L. Gomes, D. Maxwell, S. Zamani, K. Yang, D. Atienza, N. Dale, S. Mukerjee, Exploring the Role of an Electrolyte Additive in Suppressing Surface Reconstruction of a Ni-Rich NMC Cathode at Ultrahigh Voltage via Enhanced In Situ and Operando Characterization Methods, ACS Applied Materials & Interfaces 16(7) (2024) 8639-8654. https://doi.org/10.1021/acsami.3c15670.
[37] Y. He, Z. Chen, Y. Zhang, Strategies for improving cathode electrolyte interphase in high-performance dual-ion batteries, iScience 27(8) (2024) 110491. https://doi.org/10.1016/j.isci.2024.110491.
[38] J. Zhan, Y. Deng, Y. Gao, J. Ren, Y. Liu, R. Shun, W. Li, Z. Gao, Y. Chen, A Review on Low-Temperature Performance Management of Lithium-Ion Batteries, Journal of Electrochemical Energy Conversion and Storage 21 (2023) 1-37. https://doi.org/10.1115/1.4063611.
[39] H. Wang, H. Wang, S. Chen, B. Zhang, G. Yang, P. Gao, J. Liu, X. Fan, Y. Huang, J. Lin, Z. Shen, A Depth-Profiling Study on the Solid Electrolyte Interface: Bis(fluorosulfuryl)imide Anion toward Improved K+ Storage, ACS Applied Energy Materials 2(11) (2019) 7942-7951. https://doi.org/10.1021/acsaem.9b01428.

Open Access Article. Published on 22 June 2026. Downloaded on 6/23/2026 5:02:46 AM.
This article is licensed under a Creative Commons Attribution-NonCommercial 3.0 Unported Licence.

Chemical Science Accepted Manuscript

View Article Online
DOI: 10.1039/D6SC03512D

Data Availability Statement

The data that support the findings of this study are available from the corresponding author, Dr. Montree Sawangphruk, upon reasonable request.

Open Access Article. Published on 22 June 2026. Downloaded on 6/23/2026 5:02:46 AM.
This article is licensed under a Creative Commons Attribution-NonCommercial 3.0 Unported Licence.

Chemical Science Accepted Manuscript